

Research Article

Fatigue Damage Identification by a Global-Local Integrated Procedure for Truss-Like Steel Bridges

Marianna Crognale ¹, Francesco Potenza ², and Vincenzo Gattulli ¹

¹Department of Structural and Geotechnical Engineering, Sapienza University of Rome, Via Eudossiana 18, Rome 00184, Italy

²Department of Engineering and Geology, University G. d'Annunzio of Chieti-Pescara, V.le Pindaro 42, Pescara 65127, Italy

Correspondence should be addressed to Marianna Crognale; marianna.crognale@uniroma1.it

Received 5 October 2022; Revised 31 March 2023; Accepted 5 April 2023; Published 4 May 2023

Academic Editor: Zoran Rakicevic

Copyright © 2023 Marianna Crognale et al. This is an open access article distributed under the Creative Commons Attribution License, which permits unrestricted use, distribution, and reproduction in any medium, provided the original work is properly cited.

Civil steel structures and infrastructures, such as truss railway bridges, are often subject to potential damage, mainly due to fatigue phenomena and corrosion. Therefore, damage detection algorithms should be designed and appropriately implemented to increase their structural health. Today, the vast amount of information provided by data processing techniques and measurements coming from a monitoring system constitutes a possible tool for damage identification in terms of both detection and description. For this reason, the research activity aims to develop a methodology for a preliminary description of the damage in steel railway bridges induced by fatigue phenomena. The proposed approach is developed through an integration of global and local procedures. At the global scale, vibration-based procedures will be applied to improve a forecast numerical model and, subsequently, to identify the zones most involved in fatigue problems. At the local scale, careful and refined local identification will be pursued via image processing techniques whose evidence will be analyzed and described through nonlinear numerical models. A case study of a historical railway bridge in Spain will illustrate the methodology's performance, potentiality, and critical issue.

1. Introduction

To understand the behavior of complex engineering structures, Structural Health Monitoring Systems, SHMSs, are widely implemented in the fields of aerospace, civil, and mechanical engineering. In the last decades, there has been a growing interest in damage identification procedures based on changes in modal parameters, thanks to the development of a large number of algorithms that aim at providing continuous monitoring using vibration measurements for the automatic identification of dynamic parameters in operating conditions. Many researchers working in the field of SHM have focused extensively on data analysis, including feature extraction and data fusion, to identify and assess the damage. Based on the vibration features, the damage identification methods are classified into four major categories: natural frequency-based methods, mode shape-based methods, curvature mode shape-based methods, and methods using both mode shapes and frequencies.

Following is a detailed and critical overview of the available methods for structural monitoring and damage detection in truss structures, with particular attention to steel railway bridges.

It is known that Structural Health Monitoring methods measure structural response and aim at effectively detecting, locating, and assessing damage produced by severe loading actions and by progressive environmental deterioration. In the SHM process, damage identification is a critical point especially when it relates to railway infrastructures. In the infrastructural context, it refers to the estimation of the variation of some parameters, which could have a negative effect on the structural behavior. The health state of railway bridges is mainly evaluated by visual inspections and nondestructive regularly conducted tests, which can be subjective and dependent on expert knowledge. Therefore, the problem of deepening and developing methods for damage assessment in railway bridges remains open [1, 2]. In recent decades, several authors have focused on the

development of a damage identification procedure based on the vibration data analysis, in addition to the classic in situ inspections, and they have reviewed the existing literature on this field, classifying it for the different types of railway bridges. Examples of these publications include Meherjo et al. [3]; Scianna and Christenson [4]; Lu and Liu [5]; Moaveni et al. [6]; Scott et al. [7]; and You et al. [8]. Many railway bridge SHM researchers focused on numerical and experimental simulations of bridge beams and truss structures. In 2012, Beskhyroun et al. propose a method based on wavelet transforms using dynamic responses recorded under excitation applied by an actuator, but this procedure shows some limitations under operating conditions [9]; Bowe et al. presented in 2015 a method that exploits the analysis of the acceleration of vehicles resulting from the train-track interaction, but this method is not applicable in the presence of noise [10]; in the same year Gonzales and Karoumi studied a strategy based on artificial neural networks (ANN) but the limits of this methodology lie in modeling the railway bridge as a simply supported beam that does not describe the complexity of the structure [11]. A review of the latest literature is listed in the bibliography [12–21]. It is known that most of these methods have identified the existence of damage (the first level of the SHM process), without fully reaching the goal of level 2 which is the localization of damage. For applications of SHM to the case of truss structures, there are still many difficulties. Modal parameters, natural frequencies, and mode shapes are sensitive indicators of structural damage. However, they also show a high sensitivity to environmental and operational conditions such as humidity, wind, temperature, presence and measurement of noise, and accuracy of the measurements. For civil engineering structures, these variables interfere with the assessment of damage identification and sometimes even hide variations in damage indicators produced by the damage. Furthermore, the identification of modal parameters could be difficult for structures with couple-mode shapes. On the other hand, the global nature of the modal parameters extracted from the measured data recorded by accelerometers or displacement sensors may not always lead to truss damage localization and quantification [22]. As with most inverse problems, the search for a solution is complicated due to the ill-conditioning nature of the problem, since it strongly depends on the quantity and quality of the experimental data available [23, 24]. Another aspect of difficulty concerns the modeling of damage. In this work, a linear behavior is assumed, both before and after the damage; the damage is therefore thought of as an open crack or a decay of the mechanical properties and it is described by a local decrease in the stiffness of a truss element.

The growth of innovative technologies in mechatronics, robotics, and information and communication technology (ICT) is opening up new perspectives in recent years in addressing the classic problems of infrastructure management [25]. Many rising research fields could have an important impact on infrastructure inspection and monitoring, e.g., automated inspection based on image acquisition [26]. In fact, the use of mobile robots and unmanned aerial vehicles (UAVs) has strongly encouraged the development of

image acquisition techniques to describe the spatial characteristics of the environment, allowing the creation of 3D points cloud. Regarding cracks in steel infrastructures, the most common difficulties depend on the random shape and irregular size of the crack, and on the presence of noise in the acquired images (irregularities in lighting conditions, shadows, and imperfections). In general, image processing-based crack detection methods are classified into four categories [27]: integrated algorithm methods, methods with a morphological approach, percolation-based methods, and practical techniques. Many research works based on the use of a digital camera can be found in the available literatures: Talab et al. [28] presented a three-step methodology that involves the conversion of the image to grayscale and the use of the Sobel filter to detect cracks, the application of appropriate thresholds to distinguish foreground and background, and finally the application of the Sobel filter for the elimination of residual noise; Adhikari et al. [29] developed an integration model that numerically represents defects through a neural network; Alam et al. [30] proposed a detection technique by combining the DIC (digital image correlation) and acoustic emissions. Many works based on image analysis to detect the presence of damage due to crack and corrosion phenomena exploit the radiographic examination of metallic materials by X-ray and γ -ray, among them Zhang et al. [31] proposed a new damage detection system based on X-ray images, introducing its digital imaging technology, system structure, and operating principles and Peng et al. [32] used a bridge cable detection system based on γ -ray images.

Some of the main drivers for the present research include the key role that bridges play within the railway network, the increase in the use of railway infrastructure due to economic globalization and the consequent growth in traffic volume, the design speed of existing lines, and more important, the effects that this continuous increase in operational conditions can have on the bridge structural performance and service life. Existing riveted steel bridges represent an architectural heritage of great importance in Europe. Generally, railway bridges built at the beginning of the XX Century were designed without rules dedicated to the fatigue resistance of detail. For this reason, they show a marked state of degradation mainly due to corrosion and/or fatigue. Links represent the part most susceptible to these phenomena.

This research addresses the problem of identification and quantification of structural damage in steel truss bridges in relation to their intensity, location, and extent, through a classical vibration-based procedure in combination with new image processing techniques. At the global level, the damage was identified through pseudoexperimental data solving the inverse problem using a data-driven procedure in the time domain, the stochastic subspace identification (SSI), [33, 34] to determine the structure modal properties. The problem of identifying structural damage in a steel truss is firstly addressed via both a sensitivity analysis and the minimization of an objective function. In this respect, firstly, a global general model of a plane steel truss has been used to highlight the effects of different positions, extensions, and magnitude of damage on the main dynamic properties

(frequency and mode shapes). Deriving the FEM model of the damaged truss, in which damage is modeled as a cross-section reduction in a single element, a damaged stiffness matrix has been calculated. The analytic expression has shown that intensity and extent are not independent factors. Therefore, the inverse problem has been addressed to evaluate the so-called stiffness reduction factor (SRF). The used objective function is based on the error between eigenfrequencies from the numerical model and modal frequencies from pseudoexperimental testing. Subsequently, the global analysis is applied to the selected case study, the Quisi Bridge, a historical steel railway bridge located in Spain, that was analyzed by means of experimental/numerical analysis. The identification of the structural real dynamic behavior was carried out through experimental “in-field” tests using ambient vibrations by means of SSI; based on updating procedures it is possible to calibrate the numerical model concerning the experimental data. The updated model is used to locate the critical connections where fatigue damage could arise, which are then analyzed through local models. The local models have been obtained selecting on the updated global model, the critical details most exposed to fatigue problems to properly reproduce the local dynamic behavior of the details. The local analysis of connections is carried out in order to identify other parameters which can describe the damage and can be utilized at a global scale for the definition of the error function. The final part refers to the image acquisition campaign and processing in order to extract some useful information and characterize the current health state of joints. The non-destructive tests were carried out through on-site γ -rays image acquisition and processing, and the results of radiographic tests enrich the description of the damage. The final aim of the local analysis is to introduce parameters able to describe damage with high accuracy to update the global model.

The text is organized as follows: the inverse analysis of a general mono-dimensional model obtained via SSI is described in Section 2, while the global analysis of the selected case study, and the experimental dynamic tests, are presented in Section 3. Section 4 focuses on the numerical local models of the selected critical details and it includes local analysis; finally, Section 5 concerns the image acquisition and processing obtained throughout segmentation. Concluding remarks are provided in Section 6.

2. Inverse Analysis on a Simplified Model

The steel truss nominal model (STNM) consists of a 21 degree of freedoms simply supported truss, Figure 1(a), on which the effects of several damage scenarios have been assessed. The structural damage has been modeled as an axial stiffness reduction, Figure 1(b), and its intensity, position, and extent have been described introducing three dimensionless parameters ζ , α , and δ , respectively, which read as follows:

$$\zeta = \frac{EA - EA_d}{EA}, \alpha = \frac{(L_1 + L_d/2)}{L}, \delta = \frac{L_d}{L}, \quad (1)$$

where EA and EA_d are the undamaged and damaged axial stiffness, L_1 and L_d are the two lengths shown in Figure 1(b) describing the damage position, and L is the total length of the element. A damaged element stiffness matrix \mathbf{K}_d^e has been derived using the finite element method, as reported in equation (2). Equation (3) defines the Stiffness Reduction Factor SRF expressed by the coefficient Γ . Γ is described by a combination of the two parameters ζ and δ . Different combinations of these two parameters provide the same variation in frequencies and the same value of the SRF. Therefore, the two parameters are not independent [35–37]. In the undamaged case, ($\alpha = 0$, $\delta = 0$, and $\zeta = 0$) equation (2) describes the classical stiffness matrix for a truss element.

$$\mathbf{K}_d^e = \frac{EA}{L} \cdot \frac{(1 - \zeta)(1 + \delta\zeta - \zeta)}{[(1 - \zeta)(1 - \delta) + \delta]^2} \begin{bmatrix} 1 & 0 & -1 & 0 \\ 0 & 0 & 0 & 0 \\ -1 & 0 & 1 & 0 \\ 0 & 0 & 0 & 0 \end{bmatrix} \quad (2)$$

$$= \frac{EA}{L} \Gamma(\zeta, \delta) \mathbf{K}^e,$$

$$\text{SRF} = \Gamma(\zeta, \delta) = \frac{(1 - \zeta)(1 + \delta\zeta - \zeta)}{[(1 - \zeta)(1 - \delta) + \delta]^2}. \quad (3)$$

2.1. State-Space Modeling. The linear dynamic structural behavior can be fully characterized by the main modal parameters: frequencies and mode shapes. The system dynamics is governed by a set of ordinary differential equations of motion for multidegree-of-freedom structural systems (n-ODEs) in the time domain that has been derived directly from the d’Alembert principle as reported in compact matrix form in the following equation:

$$\mathbf{M}\ddot{\mathbf{u}}(t) + \mathbf{C}\dot{\mathbf{u}}(t) + \mathbf{K}\mathbf{u}(t) = \mathbf{M}\mathbf{h}w(t), \quad (4)$$

where \mathbf{M} , \mathbf{C} , and \mathbf{K} are the mass, damping, and stiffness matrices, $\mathbf{u}(t)$, $\dot{\mathbf{u}}(t)$, and $\ddot{\mathbf{u}}(t)$ are the configuration vectors containing the nodal relative displacements, velocities, and accelerations, respectively, depending on time t . The vector \mathbf{h} is the allocation vector that indicates in which nodes and directions of the nominal model of the truss system, the external excitation is applied, $w(t)$ is a stochastic white noise-type process (WN). It was considered a classical Rayleigh damping which is a viscous damping that is proportional to a linear combination of mass and stiffness according to equation (5). The two coefficients of proportionality have been determined by the damping ratio ξ that can be assumed for all modes equal to 1.5% for railway bridges [38]. These coefficients are set to $a_0 = 1.43$ and $a_1 = 1.16$.

$$\mathbf{C} = a_0\mathbf{M} + a_1\mathbf{K}. \quad (5)$$

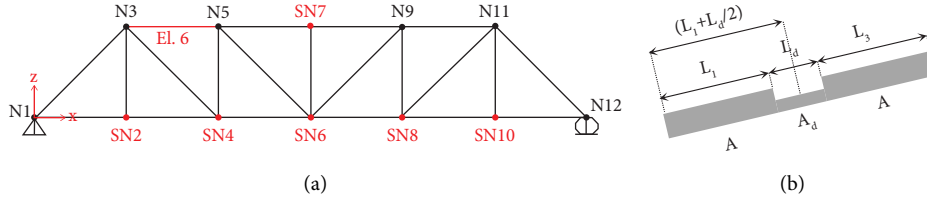


FIGURE 1: Illustration of (a) 21-DOFs STNM and (b) damage description in a truss element.

The equation of dynamic equilibrium will be converted into a more suitable form: the state-space formulation, equation (6), to convert the differential equations governing the dynamic problem into a set of first-order equations. The state-space model originates from control theory, but it also appears in mechanical/civil engineering to compute the modal parameters of a dynamic structure with a general viscous damping model.

$$\begin{cases} \dot{\mathbf{x}} = \mathbf{A}\mathbf{x} + \mathbf{B}w, \\ \mathbf{y} = \tilde{\mathbf{C}}\mathbf{x}, \end{cases} \quad (6)$$

where \mathbf{x} is the space-state vector containing nodal displacements and velocities, \mathbf{A} , \mathbf{B} , and $\tilde{\mathbf{C}}$ are the state-space matrices. $\tilde{\mathbf{C}}$ is the output matrix and it appropriately selects which state variables of \mathbf{x} will be read in the output vector \mathbf{y} . Therefore, vector \mathbf{y} could contain arbitrary pseudomeasured parameters representative of the system. For this simulation, \mathbf{y} will contain nodal vertical accelerations. In the general model described in equation (6), the state space vector and the matrices take on the following expressions:

$$\mathbf{x} = \begin{bmatrix} \mathbf{u}_{21 \times 21} \\ \dot{\mathbf{u}}_{21 \times 21} \end{bmatrix}, \mathbf{A} = \begin{bmatrix} \mathbf{0}_{21 \times 21} & \mathbf{I}_{21 \times 21} \\ (-\mathbf{M}^{-1}\mathbf{K})_{21 \times 21} & (-\mathbf{M}^{-1}\mathbf{C})_{21 \times 21} \end{bmatrix}, \mathbf{B} = \begin{bmatrix} \mathbf{0}_{21 \times 1} \\ \mathbf{h}_{21 \times 1} \end{bmatrix}, \tilde{\mathbf{C}} = [(-\mathbf{M}^{-1}\mathbf{K})_{21 \times 21} \quad (-\mathbf{M}^{-1}\mathbf{C})_{21 \times 21}]. \quad (7)$$

The SSI method identifies matrices in the state space using output-only measurements and robust numerical techniques. The dependence of the frequency on SRF is described by numerical evaluation. The procedure carried out a data processing of the pseudoexperimental response generated from the numerical model under WN. The WN is applied equally to all nodes of the system (in the two directions X and Y) to evaluate vertical accelerations in both undamaged and damaged configurations, in six sensor nodes (SN i) highlighted in red in Figure 1(a). The six nodes are selected observing the first mode shapes of the truss to avoid zero-modal points and the position SN7 has been added for redundancy. The pseudoexperimental identification has been pursued through the well-known stochastic subspace identification, using MACEC, a MATLAB toolbox developed by the Department of Structural Mechanics K.U. Leuven [39].

2.2. Vibration-Based Damage Identification Using Pseudo-Experimental Data. Figure 2 shows the dynamic pseudoexperimental responses of a selected node (SN2) under WN excitation before, Figures 2(a) and 2(b), and after damage, Figures 2(c) and 2(d). The damaged element is number 6 (see Figure 1) and the damage parameters are placed equal to $\delta = 0.3$ and $\zeta = 0.5$ (SRF = 0.769). For the selected node, both acceleration time histories, Figures 2(a)–2(c), in the time domain and pseudoexperimental response in the frequency domain (FFT), Figures 2(b)–2(d), are shown. The sampling rate is 1000 Hz, and the whole pseudorecording time is 900 s. The last 2 seconds of the time

histories have been plotted on a wider scale to highlight the pseudoexperimental responses provided by the model. Frequency domain analysis is useful for pointing out frequency variations between damaged and undamaged states. Indeed, a shift of the frequencies towards lower values is well visible in the damaged configuration. Based on recorded time histories, an alternative way to identify both frequencies and mode shapes is the classical-data-driven stochastic subspace identification [40, 41] procedure in the time domain. A stabilization analysis is made by processing all the vertical nodal responses, (SN2, SN4, SN6, SN8, SN10, and SN7), and their respective diagrams are reported for undamaged, Figure 3(a), and damaged state, Figure 3(b). The SSI procedure effectively estimates the state matrix \mathbf{A} and the output matrix $\tilde{\mathbf{C}}$. The number of modes in \mathbf{A} will be equal to half the order of the model n specified a priori, which in this application was assumed to be 80. All the results have been obtained using the same damage parameters pair ($\delta = 0.3$ and $\zeta = 0.5$) for element number 6. Among the modes obtained by SSI, there are no physical (or spurious) modes that need to be separated from the physical ones. This purpose was achieved by imposing several modal validation criteria: relative differences in frequency <20%, relative differences in damping <30%, and damping range: 0 ÷ 5%. The diagrams look very clear and the frequencies that could be related to the natural modes of vibration match with the peaks of the power spectral densities (PSDs) highlighted in gray. The pseudoexperimental results obtained through FFT and SSI processing for the first six modes of vibration in percentage are summarized in Table 1, the subscripts d and u are

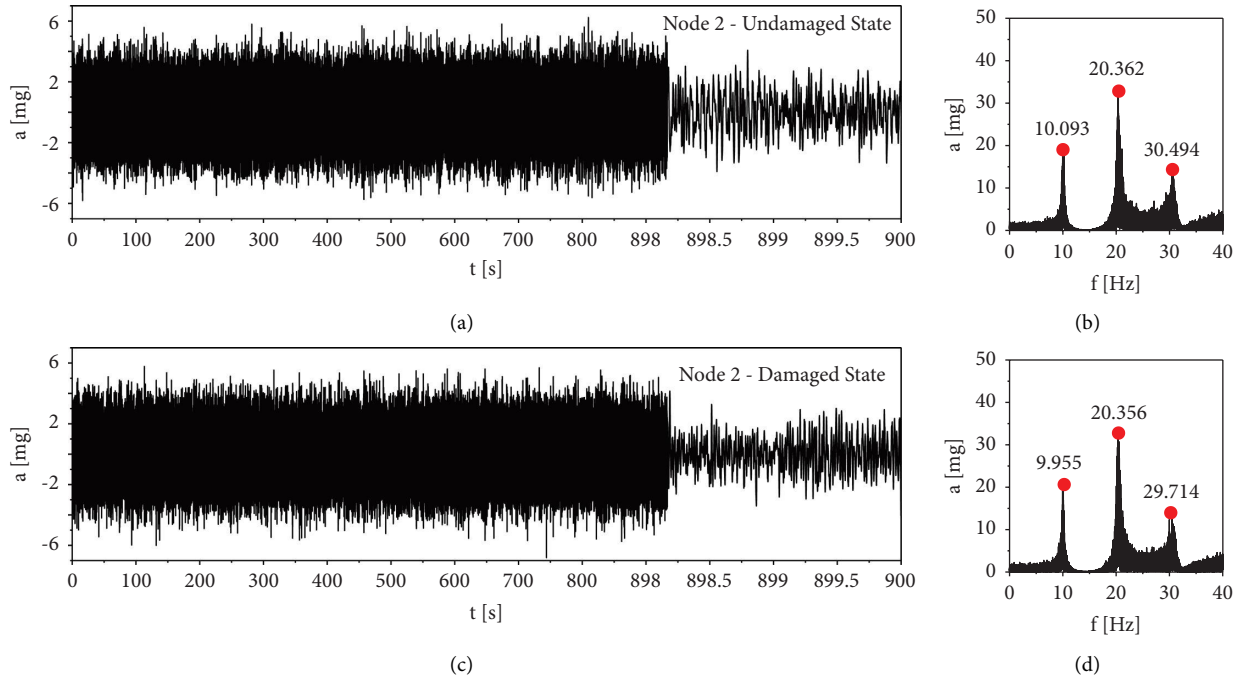


FIGURE 2: Pseudoexperimental responses under WN, from left to right: time histories and corresponding FFT, in (a, b) the undamaged and (c, d) damaged configuration. Damaged element no. 6, $\delta = 0.3$, and $\zeta = 0.5$.

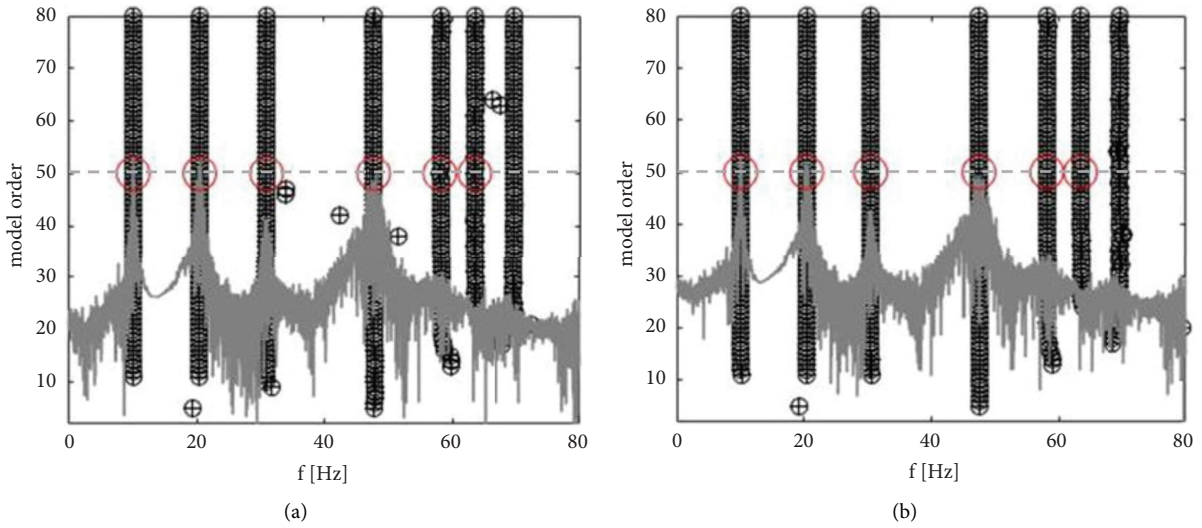


FIGURE 3: Stabilization diagrams obtained through SSI in the (a) undamaged and (b) damaged configuration. Damaged element no. 6, $\delta = 0.3$, and $\zeta = 0.5$.

TABLE 1: Frequency changes for the identified first modes of vibration (FFT and SSI).

Mode	FFT - f_u [Hz]	FFT - f_d [Hz]	FFT - Δf [%]	SSI- f_u [Hz]	SSI- f_d [Hz]	SSI- Δf [%]
1	10.093	9.955	1.37	10.045	9.935	1.11
2	20.362	20.356	0.03	20.410	20.320	0.44
3	30.494	29.714	2.56	30.820	30.352	1.54
4	-	-	-	47.855	47.562	0.62
5	-	-	-	58.360	58.274	0.15
6	-	-	-	63.605	63.547	0.09

referred to the damaged and undamaged state, respectively. It can be noted that the third mode is the most affected by the presence of damage in element 6.

Moreover, to enrich the identification process, the first six mode shapes, pre- and postdamage, were identified through SSI, and they have been compared with the numerical mode shapes obtained from the numerical FE model implemented in SAP2000. Figure 4 shows a good agreement between numerical and pseudoexperimentally identified mode shapes for both undamaged, Figure 4(a), and damaged configurations, Figure 4(b).

The inverse problem of damage identification is addressed minimizing an objective function (OF) an objective function (OF) \mathcal{L} , which defines the error between eigen-frequencies from the numerical model and modal frequencies from pseudoexperimental testing after damage related to the undamaged value. Only the first six modes have been considered to determine the $\mathcal{L}(\Gamma)$ curves. The OF based on frequency measurements can be expressed in the following equation:

$$\mathcal{L}(\Gamma) = \sum_{i=1}^{nm} \left| \frac{\omega_{d,i}^{\text{PEX}} - \omega_{d,i}^{\text{NUM}}(\Gamma)}{\omega_{u,i}^{\text{PEX}}} \right|^2, \quad (8)$$

where $\omega_{d,i}^{\text{PEX}}$ and $\omega_{u,i}^{\text{PEX}}$ are the i -th pseudoexperimental frequencies identified, respectively, in the damaged and undamaged configurations. While $\omega_{d,i}^{\text{NUM}}(\Gamma)$ representing the i -th numerical frequency depending by the SRF through the two damage parameters ζ and δ . The summation operator is indexed over the number of modes nm . Thus, the damage has been modeled in a single element of the system through a fixed value of the $\overline{\text{SRF}}$, $\Gamma(\delta, \zeta)$. An optimal estimate of the damage is evaluated by parametric analysis varying δ and ζ in the damage parameters plane, and minimizing the OF concerning the a priori-defined target point $T = (\bar{\Gamma})$, $\mathcal{L}(\bar{\Gamma}): \Pi \rightarrow \mathbb{R}$. It is worth noting that the same target curve is associated with different combinations of damage parameters that are not independent, so the procedure can identify the presence of damage without providing any information about its exact location into the damaged element. Figure 5 shows the performance of index \mathcal{L} varying the number of considered modes (the curve associated with the first mode is shown in a dotted line, the curve obtained considering the first three modes is shown in a dash-dot line, and the continuous line is associated to the first 6 modes) and the position of the damaged element (2, 5, and 6 whose position is indicated in the upper part of Figures 5(a)–5(c), respectively). These three graphs plot the value of the objective functions defined in equation (8) varying the SRF. For this simulation, the true value, (SRF = 0.769), is indicated by a vertical line in black. All the numerical results are summarized in Table 2 to highlight the performance of the \mathcal{L} index in detecting the SRF varying the number of considered modes. It is noted that an increase of modes doesn't improve the accuracy of the result and the number of modes needed to achieve a closer solution to the real value of SRF depends on which member of the truss is affected by the damage.

The obtained results quantify the influence of the SRF (the factor depending on damage intensity and extension) in the modal features of a truss structure through different indicators. Other procedures could be applied to detect the damage

position, i.e., a flexibility-based approach using the damage locating vectors (DLVs) [42, 43] has been applied to the plane analytical model previously described. The DLVs are a special set of linear independent (LI) load vectors, which if it is statically applied to the structure, is capable of producing "zero stress" in damaged elements. This unique feature makes them suitable for damage localization. The procedure initially involves the determination of the flexibility matrices in the pre- and post-damage state, indicated respectively with \mathbf{F}_U and \mathbf{F}_D and their difference with $\mathbf{F}_\Delta = (\mathbf{F}_D - \mathbf{F}_U)$. To determine the load vectors which produce identical deformations in the undamaged and the damaged states, we imposed the following equality:

$$\mathbf{F}_d \mathbf{L} = \mathbf{F}_u \mathbf{L}, \quad (9)$$

where \mathbf{L} is the matrix collecting the individual load vectors which produces the following equation:

$$(\mathbf{F}_d - \mathbf{F}_u) \mathbf{L} = \mathbf{F}_\Delta \mathbf{L} = \mathbf{0}. \quad (10)$$

Equation (10) is satisfied in two cases: if $\mathbf{F}_\Delta = \mathbf{0}$ (trivial solution), this implies that there is no damage or that the damage is limited to a region of the structure where the stresses are zero for any load condition described by the \mathbf{L} matrix; if $\mathbf{F}_\Delta \neq \mathbf{0}$ and the rank of \mathbf{F}_Δ is not maximum, \mathbf{L} represents a basis of null space for the matrix \mathbf{F}_Δ computed by singular value decomposition (SVD).

$$\begin{aligned} \mathbf{F}_\Delta &= \mathbf{U} \mathbf{S} \mathbf{V}^T \\ &= [\mathbf{U}_1 \quad \mathbf{U}_0] \begin{bmatrix} \mathbf{S}_1 & \mathbf{0} \\ \mathbf{0} & \mathbf{0} \end{bmatrix} [\mathbf{V}_1 \quad \mathbf{V}_0]^T, \end{aligned} \quad (11)$$

$$[\mathbf{F}_\Delta \mathbf{V}_1 \quad \mathbf{F}_\Delta \mathbf{V}_0] = [\mathbf{U}_1 \mathbf{S}_1 \quad \mathbf{0}], \quad (12)$$

$$\mathbf{L} = \mathbf{V}_0. \quad (13)$$

The property of the vectors in \mathbf{L} that is relevant for damage localization is the fact that these vectors when treated as loads on the system, lead to stress fields that are zero over the damaged elements. Finally, the normalized cumulative stress, NCS, of each element of the structure is calculated, deriving from the application to the undamaged analytical model of the force vectors \mathbf{L} previously obtained by the SVD. The most likely damaged element has NCS equal to zero, Figure 6.

$$\text{NCS} = \frac{\sigma_j}{\max_k(\sigma_k)}, \quad (14)$$

where

$$\sigma_j = \sum_{i=1}^{n\text{DLVs}} \text{abs} \left(\frac{\sigma_{ij}}{\max_k(\sigma_{ik})} \right). \quad (15)$$

3. Global Analysis: Application to Quisi Bridge

In the case of existing steel bridges, the actual bridge structural performance under train passage is investigated via global analysis. Numerical FE global models lead to a reliable assessment of internal forces in bridge components. The Quisi

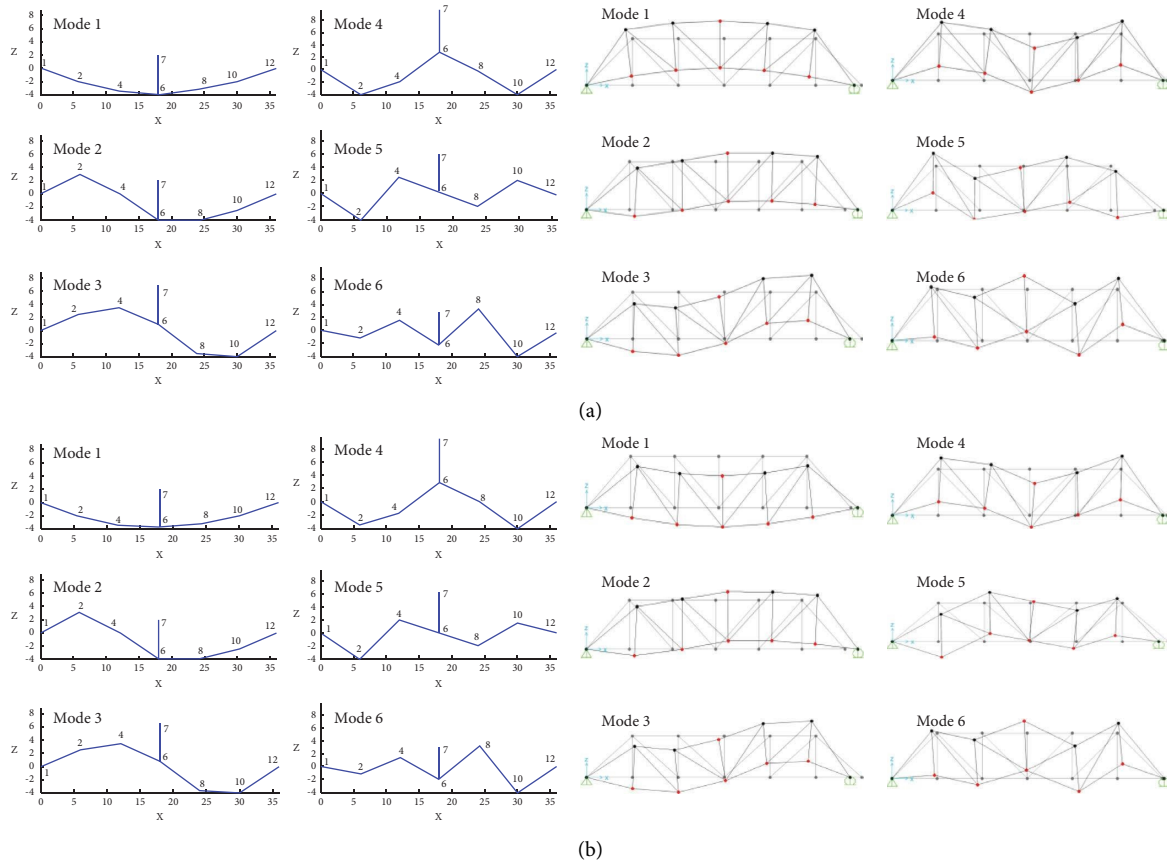


FIGURE 4: Comparison between identified and numerical mode shapes in the (a) undamaged and (b) damaged state.

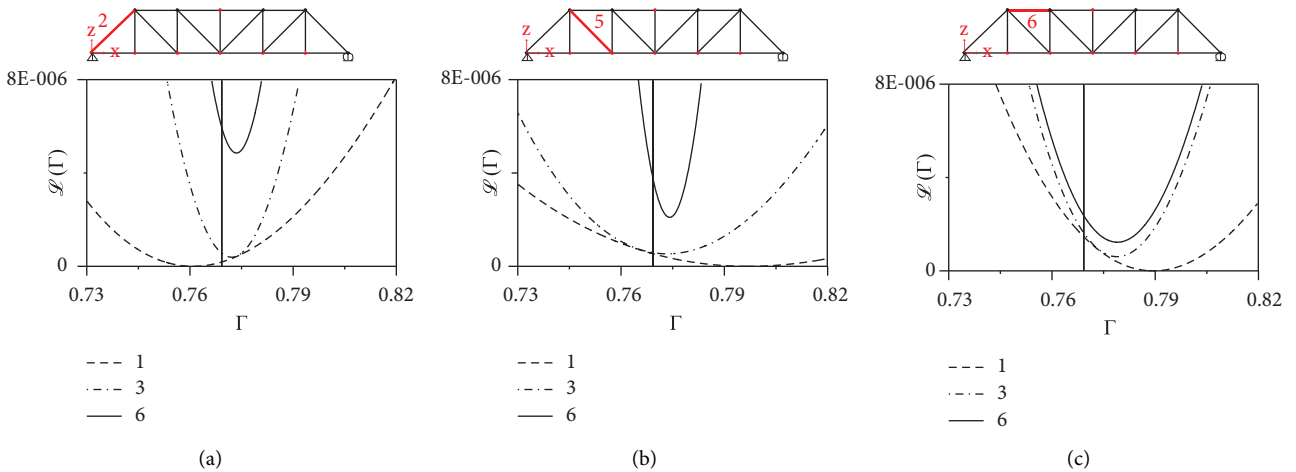


FIGURE 5: Effects of the number of modes in the determination of Γ value, respectively, for damaged elements (a) 2, (b) 5, and (c) 6.

Bridge is a historical steel truss railway bridge from the XX century, located in Spain (Benissa, Alicante) and it is part of the 9th FGV Railway Line [44]. The bridge was built in 1917 and the structure consists of a top-bearing Pratt-type truss, entirely riveted, Figures 7(a) and 7(b). According to the structural system of a Pratt-type truss under uniform distributed loads, the upper chord is in compression and the lower chord is in a tension state. The deck of the Quisi viaduct houses a single-track railway line, centered on the entire

length of the bridge. The deck structure has cross bracing in both transversal and horizontal plans. Longitudinally, the bridge is composed of two central continuous main spans, each of them is 42.00 m long, and four side simply supported spans, (two of 21.48 m and two of 21.12 m), forming a bridge total length of 170 m, Figure 7(c). The isostatic spans are restrained by alternating hinged and roller connections, and the continuous span is restrained by hinged support in the middle and two roller supports at both ends. The substructure

TABLE 2: Performance of the OF \mathcal{L} in the identification of the SRF factor.

Mode	Damaged Element 2		Damaged Element 5		Damaged Element 6	
	Γ	E_r [%]	Γ	E_r [%]	Γ	E_r [%]
1	0.7609	1.08	0.7968	3.58	0.7894	2.63
2	0.7629	0.81	0.7734	0.54	0.7863	2.22
3	0.7721	0.37	0.7734	0.54	0.7789	1.26
4	0.7725	0.42	0.7737	0.58	0.7784	1.19
5	0.7733	0.53	0.7737	0.58	0.7787	1.22
6	0.7736	0.56	0.7741	0.63	0.7789	1.26

Bold indicates the minimum error between the OF and the real value of SRF.

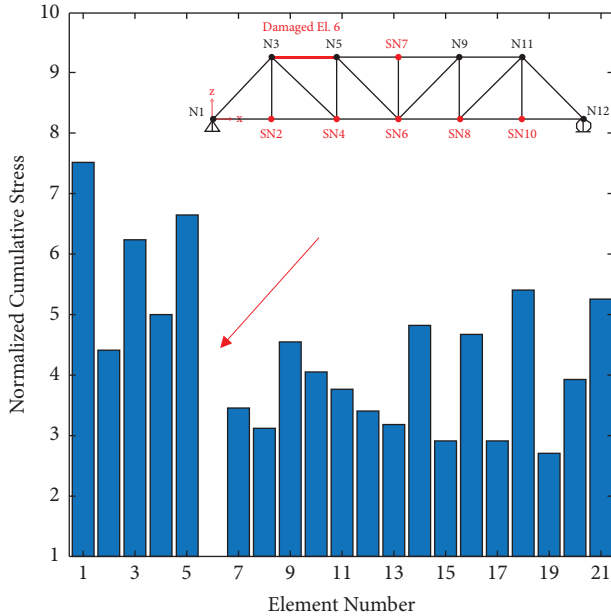


FIGURE 6: Detection of a damaged element obtained by DLVs procedure in STNM.

consists of two stone masonry abutments with square sections and five steel pylons with truncated pyramidal shapes. The pylons are made of several modules of truss structure depending on the length of the pylon. It is distinguished between two types of piles. The first group consists of the P-1, P-4, and P-5 piles, of lower height, and the second group is composed of the P-2 and P-3 piles, of greater height, Figure 7(b). Figure 7(d) shows some details of the piles and rivets. The bridge was made in structural steel, as regards the strength and the elastic modulus of the steel, the correct values have been taken from several documents consulted [45, 46]. Among these documentation, we found a steel characteristic resistance of 240 MPa (corresponding to a design strength of 90 MPa). The Quisi Viaduct has been investigated with different techniques to assess the damage produced by fatigue phenomena (dynamic tests, visual inspections with drones, and acquisition of images through γ -ray photogrammetry). The four isostatic spans have the same geometry and are independent from the two central spans constituting the main

hyperstatic truss. Therefore, each span that makes up the deck must be modeled separately. The 3D models were made in SAP2000 with beam elements connected by start-end release to create a truss system. An elastic and linear constitutive law has been adopted for the material (Steel S235) using the following nominal parameters: yield strength $f_{yk} = 240$ MPa, Young modulus $E = 210000$ MPa, specific weight $\rho = 7850$ kg/m³. Figure 8 shows the first main three mode shapes of vibration mostly involved in the vertical dynamic response for Model A, Figure 8(a), and Model B, Figure 8(b), representative of the isostatic span and the hyperstatic one, respectively. For Model A the first mode ($f_1 = 8.598$ Hz) is a vertical translation, the second mode ($f_2 = 12.701$ Hz) is torsional, and the third ($f_3 = 24.158$ Hz) is bending in the vertical plane. For Model B the first two modes ($f_1 = 4.355$ Hz and $f_2 = 5.884$ Hz) are bending in the vertical plane and the third mode ($f_3 = 7.936$ Hz) is torsional. Instead, Model B is more flexible than Model A.

3.1. Influence of the SRF on the Modal Features. The FE global model of the main span, Model B, permits to evaluate the modal features variation due to the presence of damage. Two damage scenarios are implemented and studied: the first one (DS1) affects only one element of the main span, while the second (DS2) involves a group of 14 elements, as shown in Figure 9(a). In both numerical simulations, the SRF was placed equal to 0.3 for each element. The sensibility of the first four modal frequencies related to both DSs appears to be quite low evidencing the need of introducing other types of damage index based on mode shapes. The two correlation parameters analyzed are, respectively, the MAC index and the CoMAC index [47, 48], whose expressions have been reported in the following equations:

$$\text{MAC}_{ij} = \frac{|\phi_i^d \cdot \phi_j^u|^2}{|\phi_i^d|^2 |\phi_j^u|^2}, \quad (16)$$

$$\text{CoMAC}_i = \frac{\left(\sum_{j=1}^{nm} |\phi_{ij}^d \phi_{ij}^u| \right)^2}{\sum_{j=1}^{nm} (\phi_{ij}^d)^2 \sum_{j=1}^{nm} (\phi_{ij}^u)^2}. \quad (17)$$

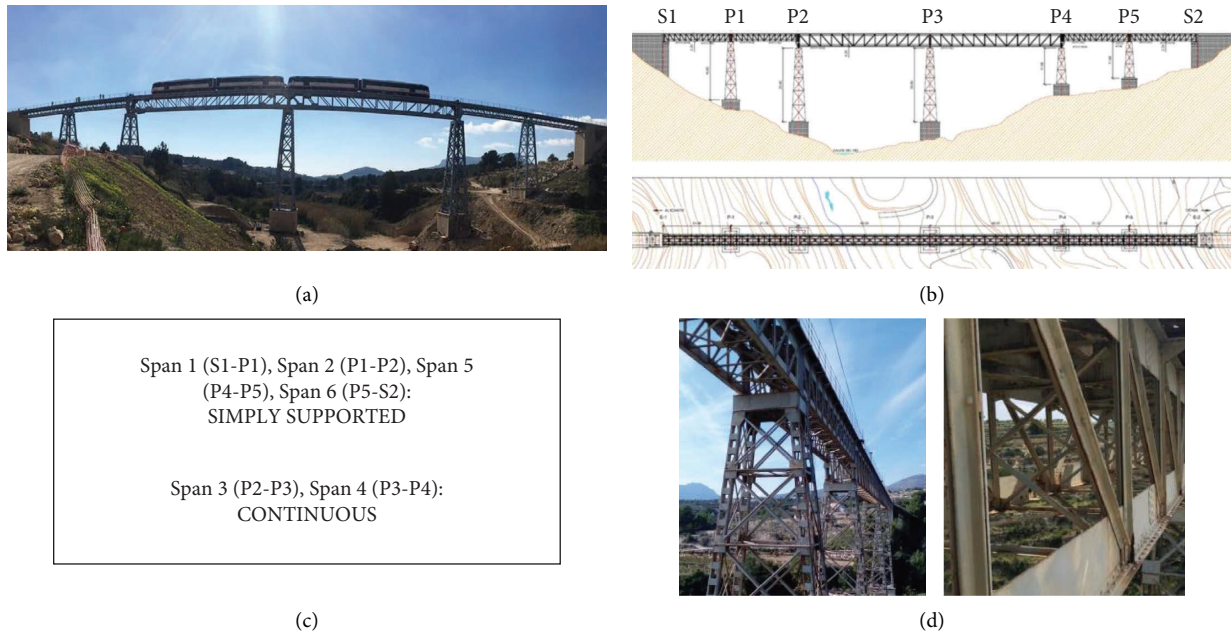


FIGURE 7: (a) General view of the Quisi bridge, (b) technical drawing of the Quisi bridge, (c) restraining condition for each span, and (d) details of the piles and rivets.

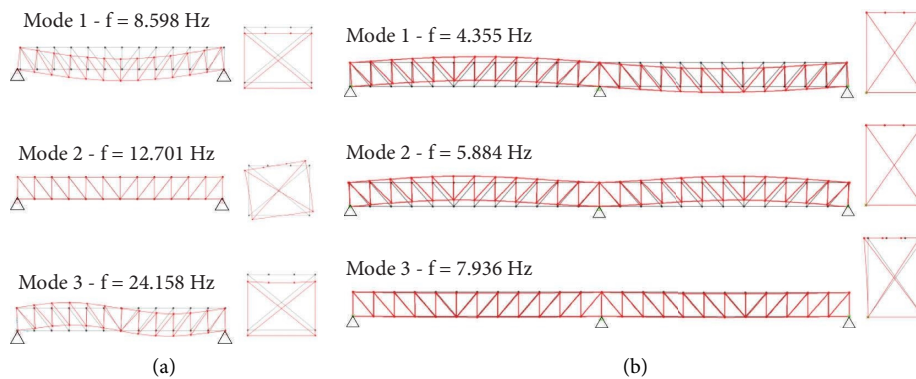


FIGURE 8: First three mode shapes for (a) model A and (b) model B.

MAC index is a real-value function that compares two sets of eigenvectors, referring to the damaged case (DS) and the undamaged one (UN). MAC always assumes a value between 0 and 1: where 0 indicates no correspondence between two eigenvectors (orthogonal eigenvectors), and where 1 indicates a perfect correlation. Figure 9(b) and Table 3 summarize the results: MAC values indicate little change in mode shape for DS1, with a MAC value larger than 0.98 for the first two modes. As a result, MAC fails to reflect the change in mode shape in the first scenario. Marked changes in mode shape are observed for DS2; the most remarkable change occurs in the sixth mode with MAC decreasing to 0.82. A second major change occurs in the first and seventh modes (MAC = 0.83). However, in both cases, MAC as a global index fails to estimate the damaged element of the truss.

The CoMAC index can be regarded as a point-wise measure of the correlation between two sets of mode shapes and be defined for a measurement point (or a degree

of freedom) I ; it permits to evaluate, for each degree of freedom, the correlation existing between two mode shapes, referring to the damaged and undamaged scenario, respectively. Also, this indicator can assume values between 0 and 1 and its tendency to unity indicates a close correlation between the modes of vibration at the point analyzed.

Figure 10 shows the CoMAC values calculated for DS1, Figures 10(a)–10(c), and DS2, Figures 10(d)–10(f), in the direction X, Y, and Z. Focusing on direction Y, the transversal direction of the truss structure, that is the most relevant from the damage detection point of view, for DS1 the CoMAC index has been affected by confusing localization. It has two absolute minimum points, located symmetrically in the truss, placed at $0.5 L$, where L represents the half length of the hyperstatic span, Figure 10(b). Therefore, CoMAC identifies exactly the damaged element but also presents a false positive in the half span where the damage has not been applied. The symmetrical trend of the index along the length is justified by the fact that the model is symmetrical in

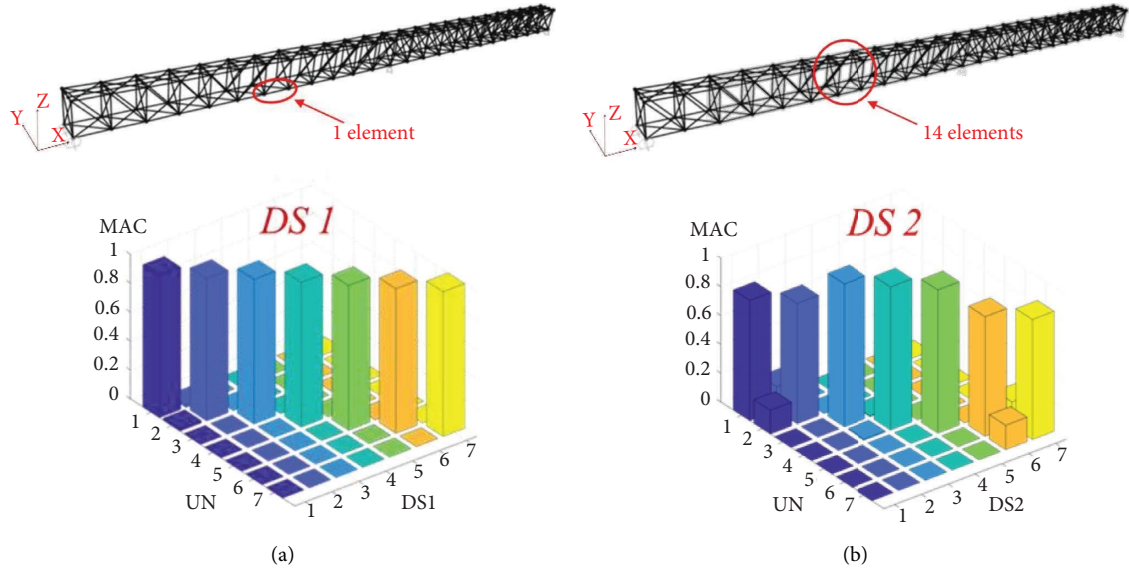


FIGURE 9: Illustration of the two damage scenarios applied to the main span and the corresponding MAC matrix (a) for the isostatic span and (b) for the hyperstatic one.

TABLE 3: MAC comparing modes from the numerical model for damaged and undamaged scenarios.

Scenario	Mode	UN						
		1	2	3	4	5	6	7
DS1	1	0.984	0.016	0.000	0.000	0.000	0.000	0.000
	2	0.016	0.984	0.000	0.000	0.000	0.000	0.000
	3	0.000	0.000	0.999	0.000	0.000	0.000	0.000
	4	0.000	0.000	0.000	0.999	0.000	0.000	0.000
	5	0.000	0.000	0.000	0.000	0.999	0.000	0.000
	6	0.000	0.000	0.000	0.000	0.000	1.000	0.000
	7	0.000	0.000	0.000	0.000	0.000	0.000	1.000
DS2	1	0.834	0.165	0.000	0.000	0.000	0.000	0.000
	2	0.165	0.835	0.000	0.000	0.000	0.000	0.000
	3	0.000	0.000	0.992	0.072	0.000	0.000	0.000
	4	0.000	0.000	0.071	0.992	0.000	0.000	0.000
	5	0.000	0.000	0.000	0.000	0.994	0.000	0.000
	6	0.000	0.000	0.000	0.000	0.000	0.829	0.167
	7	0.000	0.000	0.000	0.000	0.000	0.168	0.831

Bold indicates a value calculated with the same mode from the scenario pair.

terms of geometry and constraint conditions. Moreover, the material is elastic, linear, isotropic, and homogeneous. Also, for DS2, the CoMAC shows a low sensitivity to the presence of damage in directions X and Z . Concerning direction Y , it fails to identify the area subject to damage demonstrating an average reduction of 22% over all degrees of freedom, Figure 10(e).

3.2. Quisi Bridge Vibration Data Acquisition under Environmental Noise. For the Quisi Bridge, experimental dynamic identification of the main features characterizing the dynamic behavior of the structure was performed to calibrate the numerical global model on experimental data by updating procedures. To identify the real dynamic behavior

of the structure by experimental OMA analysis, experimental testing in environmental noise as a source of excitation was conducted. The experimental setup is shown in Figure 11(a), and it includes vertical uniaxial accelerometers in green and triaxial accelerometers in red arranged longitudinally at $0.25L$ and $0.5L$ of distance for the isostatic spans, and at $0.2L$ and $0.3L$ in the hyperstatic one. The type of sensor used is the PCB 393B31, Figure 11(b), the acquisition time is 600 s, and the sampling frequency is 200 Hz, resulting in a sampling interval of 0.005s. In order to check the validity of the recorded data, the acceleration time histories and the respective PSDs obtained with a Hanning-type window were calculated for each span of the bridge. The results for Span1 and Span3 of the viaduct are shown in

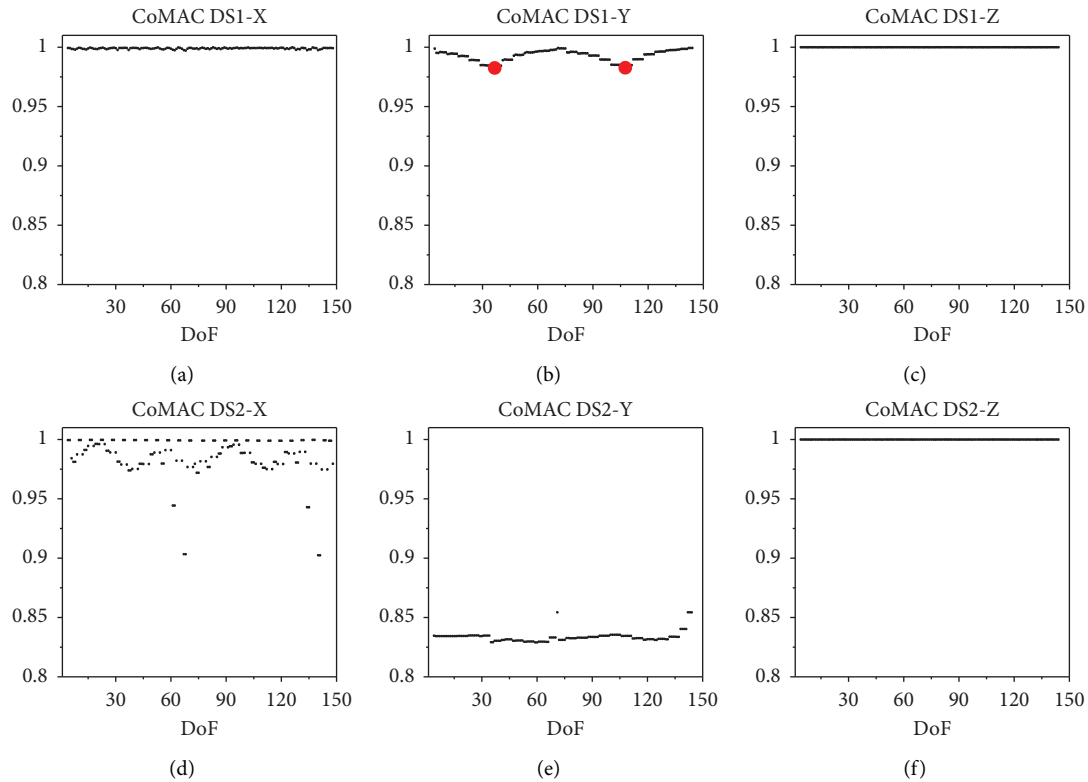


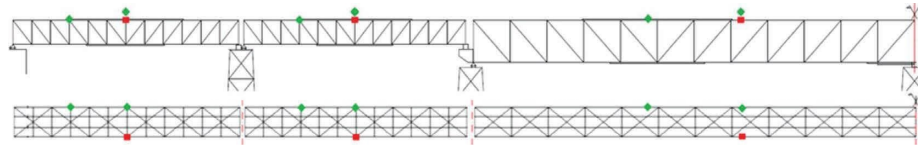
FIGURE 10: CoMAC values obtained for the (a–c) DS1 and (d–f) DS2. From left to right: direction X, Y, and Z.

Figures 12(a) and 12(b), respectively. The CH01-CH02 are related to the uniaxial sensors and the channel CH03:CH05 are related to the triaxial sensors. It should be noted that the triaxial sensors may not have worked well, therefore the impossibility of gathering significant information. Starting from the recorded data, the global modes are identified using the SSI procedure. A first elaboration was made using all the available data, (accelerometers Uni + triax), and a second one was conducted based only on data coming from uniaxial sensors, (Uni). For Span1, Figure 13(a), and for Span3-4, Figure 13(b), the stabilization diagrams obtained using both two setups, are reported. Tables 4 and 5 summarize the results in terms of frequency for the isostatic and hyperstatic spans, respectively, obtained from experimental measurements (PSDs and SSI-Data) and compared with those obtained from the numerical model. The percentage of errors between identified and numerical frequencies decreases considering only uniaxial accelerometers (errors around 5%). A manual model updating of the linear parameters (Young modulus) of the numerical model has been performed comparing only frequencies. For the manual model updating, only the data coming from the uniaxial sensors are used. The minimized parameter is the value of the frequency variation, which was made around 5%. Note that all the results contained in Tables 4 and 5 are based on the updated models. The literature [49–51] concerning the updating of finite element models through information from the experimental world is extremely rich thanks to the numerous possible applications of these techniques in different fields of engineering. A further focus on the application of updating


procedure to the Quisi bridge case study can be found in Figure 14 for the first span, where the first two modes of vibration are shown. Figure 14(a) shows the eigen modal shapes from the numerical model in perspective view whereas Figure 14(b) shows the same modal deformations in transversal and longitudinal views. Finally, the third column in Figure 14(c) shows the corresponding modal shapes obtained from the identification SSI-data. It is worth mentioning that the accuracy of mode shapes identification increases with the number of sensors available for dynamic tests; considering only uniaxial sensors, green points in Figure 14(c) makes this identification undetermined.

4. Local Analysis

The global analysis of the Quisi Bridge aims to investigate the current structural performance of the bridge under train passage, including the assessment of the distribution of internal stresses in each critical connection in which they are maximized for live loads. The development of a global model is essential for determining the portion of the structure where to increase the accuracy through a detailed local model. The correct evaluation of local effects, generally neglected or simply not considered by standard mechanical modeling, is one of the main issues of damage identification. These critical connections can be successfully identified by a preliminary static global linear analysis of the bridge structural behavior, employing standard analysis properly refined in order to catch a qualitative indication of local behavior. Thus, by using the updated global FE model,



(a)

	Sensitivity ($\pm 5\%$)	10.0 V/g	Broadband Resolution	0.000001 g rms
	Measurement Range	0.5 g pk	Non-Linearity	$\leq 1\%$
	Frequency Range ($\pm 5\%$)	0.1 ÷ 200 Hz	Transverse Sensitivity	$\leq 5\%$
	Resonant Frequency	≥ 700 Hz	Overload Sensitivity (Shock)	± 40 g pk

(b)

FIGURE 11: (a) Experimental setup of the acquisition system installed on the Quisi bridge in red the uniaxial sensors and in green the triaxial sensors and (b) technical specifications of the 393B31 PCB sensor.

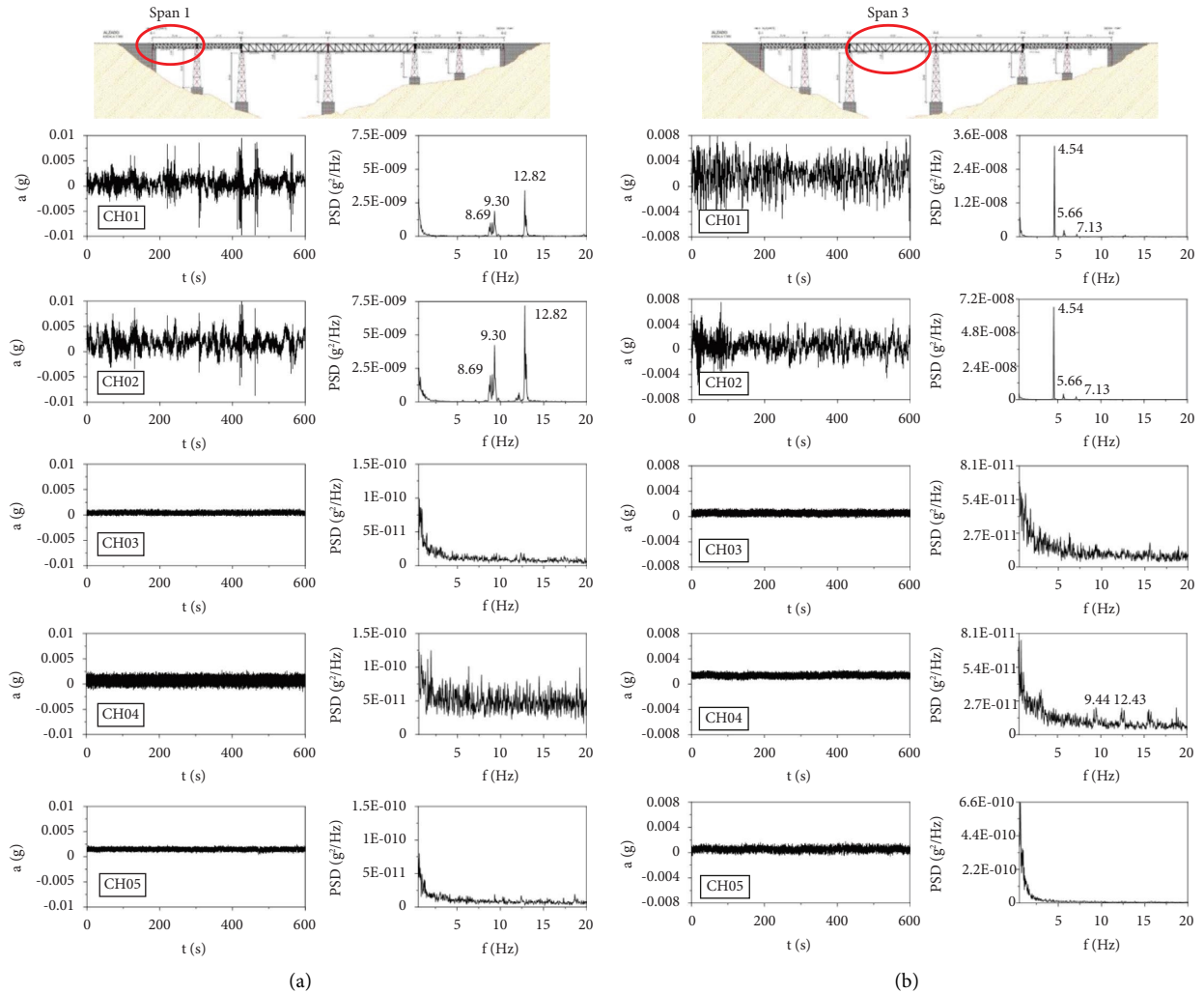


FIGURE 12: Data processing for (a) the first isostatic span and (b) the hyperstatic span.

preliminary analysis could be carried out of the overall structural behavior of the viaduct in order to obtain a qualitative assessment of the local behavior and to identify the critical portions most exposed to damage phenomena

caused by the train passages. Generally, a concentration of generalized stress, such as moment or shear, in the model should correspond to existing damages, such as cracks. These critical portions will then be analyzed by means of

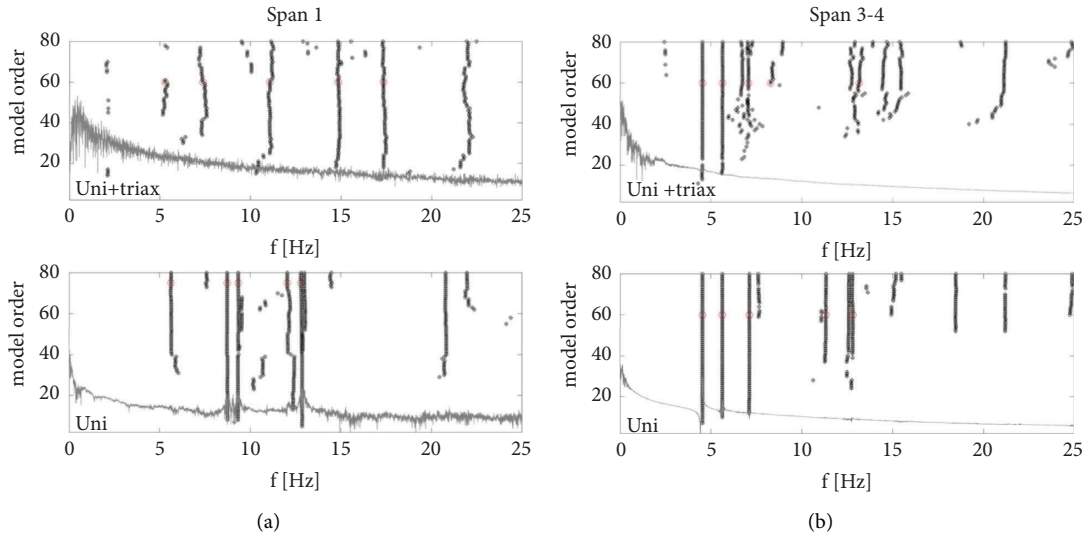


FIGURE 13: Stabilization diagrams obtained through SSI (a) for the first isostatic span and (b) for the first hyperstatic span.

TABLE 4: Frequencies experimentally identified compared with frequencies from the numerical updated isostatic span model.

Mode	PSD - f [Hz]					SSI - f [Hz]		Num	Er [%]	
	CH01	CH02	CH03	CH04	CH05	uni+triax	uni	f [Hz]	uni+triax	uni
1	-	-	-	-	-	5.282	-	-	-	-
2	8.691	8.691	-	-	-	7.368	8.733	8.590	-14.2	1.66
3	9.302	9.302	-	9.424	-	11.06	9.323	-	-	-
4	12.13	12.13	-	-	-	-	-	-	-	-
5	12.82	12.82	-	12.72	-	-	12.81	12.71	-	0.83

TABLE 5: Frequencies experimentally identified compared with frequencies from the numerical updated hyperstatic span model.

Mode	PSD - f [Hz]					SSI - f [Hz]		Num	Er [%]	
	CH01	CH02	CH03	CH04	CH05	uni+triax	uni	f [Hz]	uni+triax	uni
1	4.541	4.541	-	-	-	4.352	4.533	4.356	4.05	4.07
2	5.664	5.664	-	-	-	5.637	5.589	5.884	-4.21	-5.02
3	7.129	7.129	-	-	-	7.063	7.711	7.936	-11.1	-2.85
4	-	-	-	9.448	-	8.271	-	9.502	-12.9	-
5	-	-	-	12.43	-	13.16	12.82	13.78	-4.49	-6.96

a local analysis to assess their stress state. Proper assessment of local effects generally not considered in standard mechanical models is one of the main problems of damage identification. It is known that during the service life, many secondary components of steel truss bridges can show damage problems due to fatigue phenomena induced by distortions or vibrations. The objective of a local analysis is to obtain the correct stress distribution within the considered detail. Different simulations were carried out after the creation of the local FE models. The local numerical models developed concern of two different critical details of the Viaduct, belonging to the hyperstatic and isostatic spans that were modeled with two-dimensional finite elements and with solid finite elements, respectively. The software Midas FEA NX has been used in both cases for this purpose. For the

description of the models, please refer to the following paragraphs.

4.1. Elasto-Plastic Analysis on Local Model with 2D-FE. Figure 15 shows the area of maximum stress identified by the updated global model of the main span, at the train passage. The only train passing on this Viaduct is a series 1000 Locomotive, (Ferrocarillas de la Generalitat Valenciana), whose composition is sketched in Figure 15(a); the potential fatigue damage zone obtained from the global updated model is reported in Figure 15(b) and the critical detail identified from the model and indicated in a perspective view of the Viaduct with a red arrow is shown in Figure 15(c).

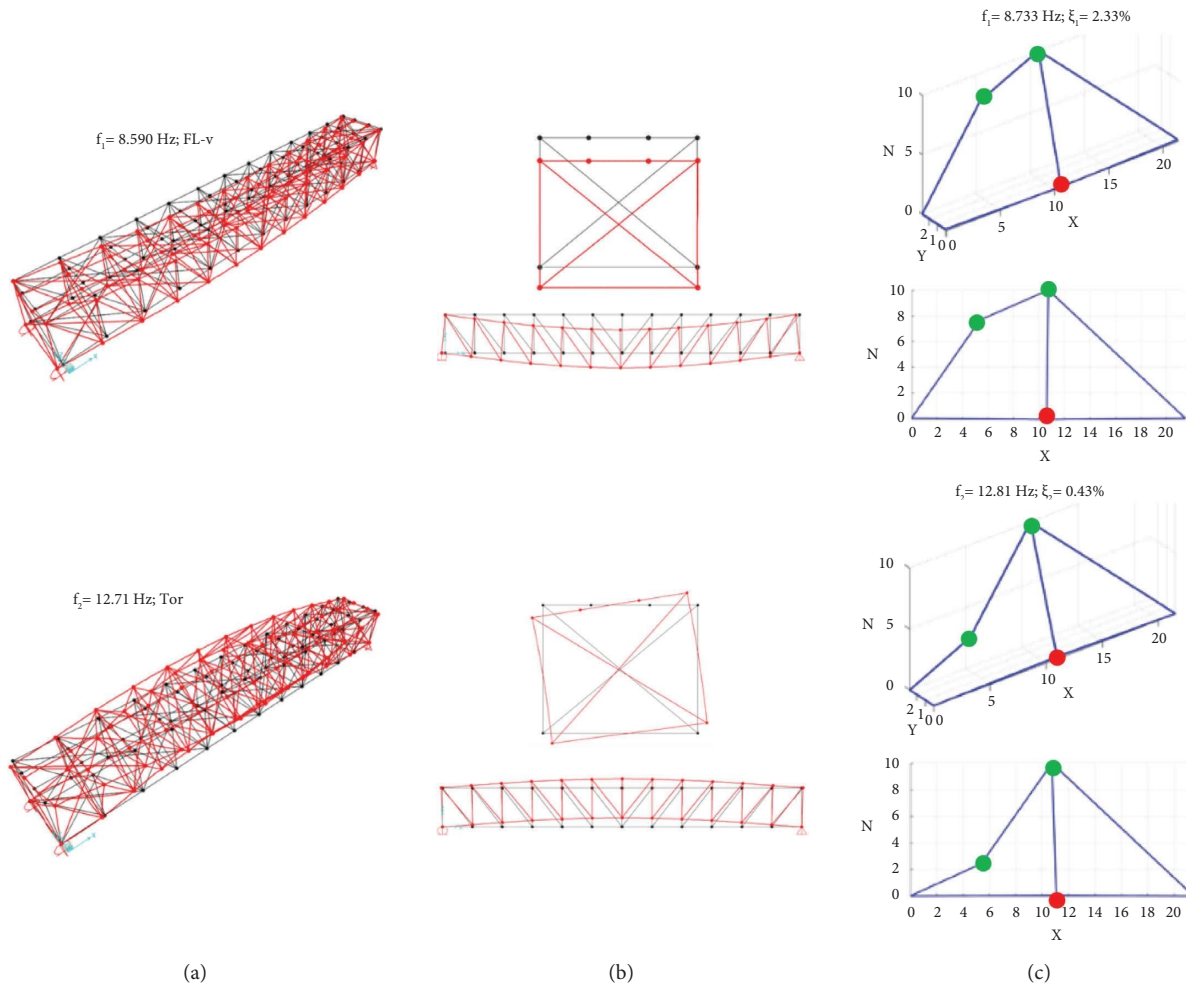


FIGURE 14: Result of the manual model updating of the isostatic span.

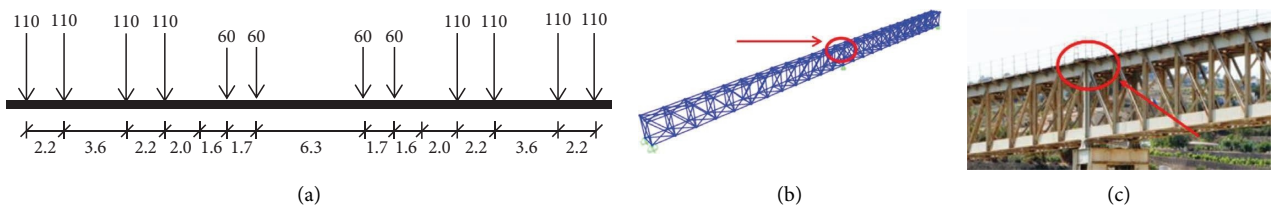


FIGURE 15: (a) Locomotive class 1000 (units kN, m); (b) zone of maximum stress from the global FE model B; and (c) detail of potential damage highlighted on the Quisi bridge.

The joint can be described as a combination of two-dimensional elements connected by the nonpenetration unilateral constraint and a link system describing the rivets. The geometric model of the joint was created and directly imported into Midas FEA NX through CAD drawing software. The plates were modeled with two-dimensional shell-type elements and subsequently, the real thickness was assigned and meshed with tetrahedral and triangular two-dimensional finite elements. These surfaces are not mutually

connected and therefore are not affected by the presence of each other; to respect the congruence this connection was made through a system of elastic links between surface nodes, with compression-only property. The rivets are modeled with beam finite elements (linear elastic constitutive law) with a circular cross-section. The master nodes of the rivet are connected to the slave nodes of the hole of the plate. The material of the plates was defined as an elastoplastic with yield surface according to the Von

Mises resistance criterion. The elastic-linear strain hardening model supposes that the continuous curve is approximated with two straight lines, the first line has a slope of Young's modulus, while the second straight line presents an idealization for the strain hardening range and has a slope which corresponds to the tangent modulus (E_t), where $E_t < E_1$. The local model is loaded with tensile forces applied in the end sections of the diagonal elements. The other elements converging in the node are hinged. Overall, the model has 150195 nodes and 217155 finite elements. Figure 16 shows some details of the local model: Figure 16(a) a perspective view of the geometry, Figure 16(b) a front and a bottom view to better appreciate the complexity of the vertical member section, and finally, Figure 16(c) a detail of the rivet modeling. The simulation presented in this chapter is a force-controlled static nonlinear SNL analysis [52]. Figures 17(a)–17(e) show the distribution of the maximum main stress in many different load steps, also reported numerically in Table 6. Analysis of the figure reveals maximum stress levels in the order of 673 MPa. The maximum stress is observed in the connecting plate. The axial force obtained from the global updated model was increased 4 times to achieve this level of plasticity in the node. In Figure 18(a) the plastic status obtained from the analysis (where the blue color indicates the plastic zones) highlights potential areas of cracking (the connection plate is a plastic region). In Figure 18(b), the detail of the double row of holes in the riveted plate is shown, only the external holes have reached the plastic state as they are more stressed. In Figure 18(c), the flow of the main stresses is highlighted by blue (compression) and red (traction) lines.

The calculation options of the nonlinear static analysis were carefully chosen, given the complexity of the model and the computational effort, appropriately calibrating for the solver number of steps, the maximum number of iterations, the convergence criterion, and the tolerance that the chosen standard must respect. Referring to the steps number, a balance was reached between analysis time and the possibility of load gradual application that does not cause convergence problems (800 steps). The iteration method adopted is the initial stiffness and it uses the stiffness matrix, calculated at the beginning of the analysis stage. Regardless of the load level, the stiffness matrix remains unchanged during the entire process of analysis. This method is used for analyses which tend to exhibit instability. As a convergence criterion, the displacement norm was adopted because it is more stable. The displacement criteria is the Euclidian norm of the iterative displacement increment. For this analysis, the CPU time took 5 days.

To reduce the CPU time a second model was created without holes and rivets but with continuous plates connected by a link system and therefore with a greater discretization step, Figures 19(a) and 19(b). The simplified model has 11424 nodes and 16040 finite elements. The shell connections were modeled through two different solutions, first using a rigid link system: the rigid link option connects two nodes with an “infinite” stiffness and it constrains

geometric relative displacements or rotations between two or more nodes of a structure. Subsequently, an elastic behavior was assigned to the link system, with high stiffness in the longitudinal direction. The shear stiffness was instead calibrated in order to reproduce a response as close as possible to the fine model. In both cases, 400 load steps were used. The second analysis is displacement-controlled and it is carried out by applying a horizontal displacement in the extremal section of the vertical element, equal to 20 mm. The CPU time took 17 h. The purpose of this analysis is to determine the capacity curve of the joint, resulting from the plasticity. The results of the comparison between the fine and simplified model in terms of capacity curves are shown in Figure 19(c), varying the number of steps. The model whose response is closest to the fine model is the one with elastic links. Finally, Figure 20 represents the evolution of the plastic status for the fine model, Figure 20(a), and for the simplified model, Figure 20(b), in four load steps corresponding to 5, 10, 15, and 20 mm of imposed displacement. Red areas map elements that are in the plastic field.

4.2. Elasto-Plastic Analysis on Local Model with Solid FE.

In the global model of the isostatic system, the critical sections identified from global linear static analysis are the supports, so the critical detail object of the local modeling with solid elements is represented in Figure 21; in Figures 21(a)–21(c), it is possible to observe the position of the node; in Figure 21(d), the views of the solid model made in CAD environment and subsequently imported into Midas FEA NX; and in Figure 21(e), the rivets modeled as cylindrical solids with hemispherical caps are shown more in detail.

Each solid geometry is made congruent through the Boolean self-connection command (Auto-Connect) and subsequently meshed with tetrahedral solid elements with an elastoplastic constitutive law with yield surface according to the Von Mises resistance criterion. The rivets too are meshed with tetrahedral solid elements. The constitutive law of the rivets is linear elastic. The modeled steel connection consists of 103078 finite elements and 51090 nodes. The self-connection command mutually constrains the geometries in contact with specific interface-type finite elements that model the unilateral contact (noncompensation constraint). Midas FEA NX provides surface interface elements, which are lower and higher-order triangular and quadrilateral elements. The surface interface elements are used to analyze the interface behavior between solid elements or between shell and solid elements. For the selected model, the interfaces are divided into flat interfaces at the contact between elements and cylindrical interfaces at the contact of the rivets with the plate hole; the interfaces are modeled with low tensile strength and without friction.

In the static nonlinear analysis, the axial forces obtained from the global model, increased by 3 times, are applied to the three diagonal elements. Figure 22 shows the distribution of Von Mises stress, respectively, on the solid, Figure 22(a), and more in detail on the three rivets of the horizontal element, Figure 22(b). The results agree with the applied

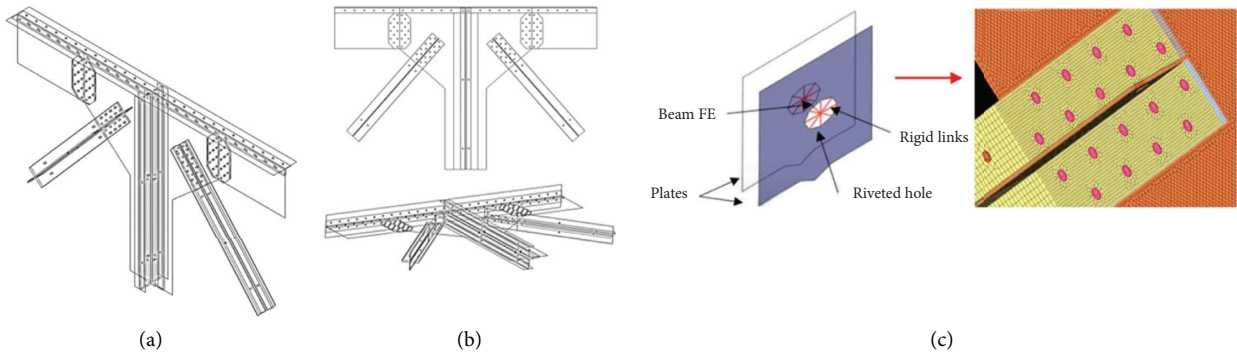


FIGURE 16: Details of the fine-meshed local model (a) in perspective view, (b) front and bottom views, and (c) the rivets modeling.

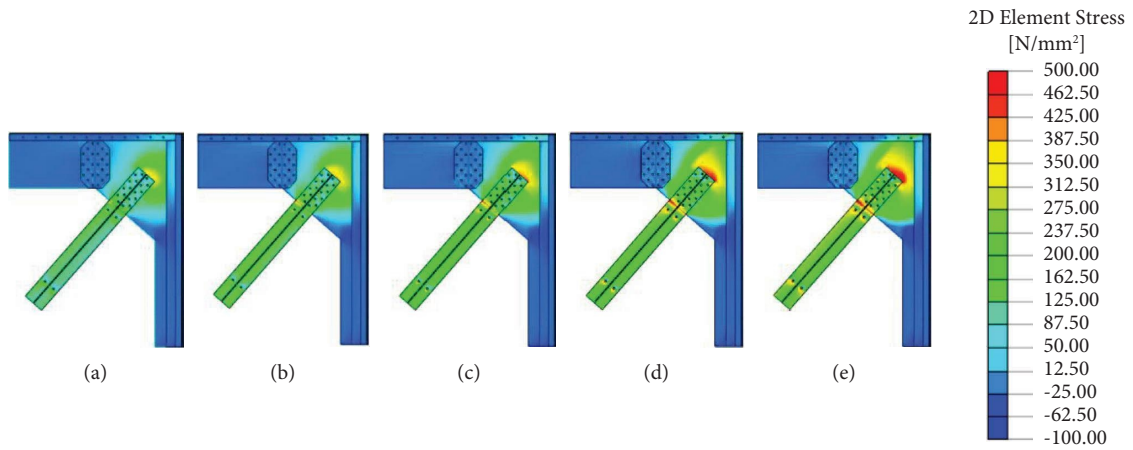


FIGURE 17: (a-e) Maximum stress obtained from SNL analysis.

TABLE 6: SNL analysis of maximum stress.

Step	T [kN]	σ_1 [MPa]
(a)	385	70.21
(b)	1155	203.1
(c)	1925	338.4
(d)	2695	472.5
(e)	3465	607.2

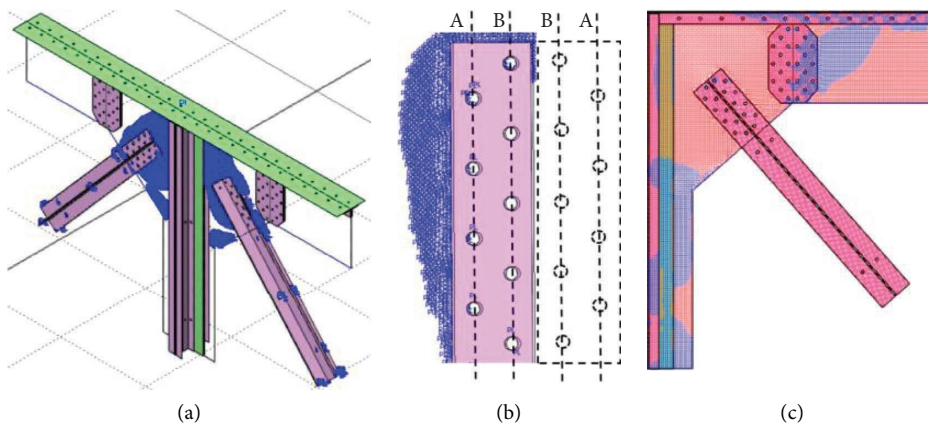


FIGURE 18: (a) Plasticity status in the analyzed node and (b) more in detail in the riveted plate. (c) Flow of the main stress.

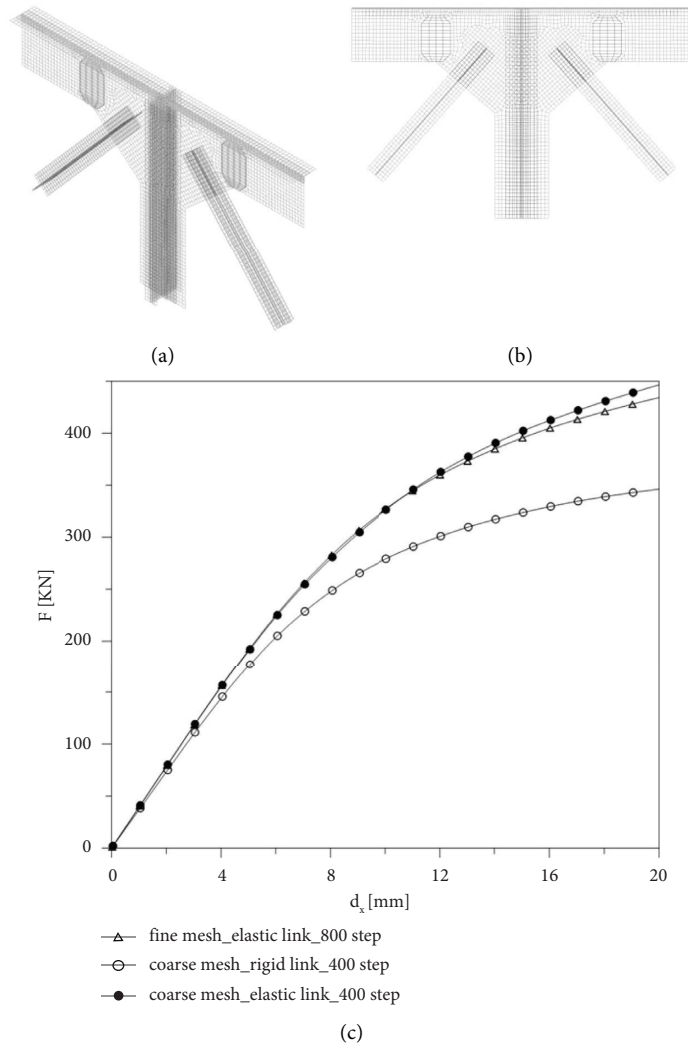


FIGURE 19: Simplified local model: (a) perspective view, (b) front view, and (c) capacity curves obtained varying the number of steps and the link definition.

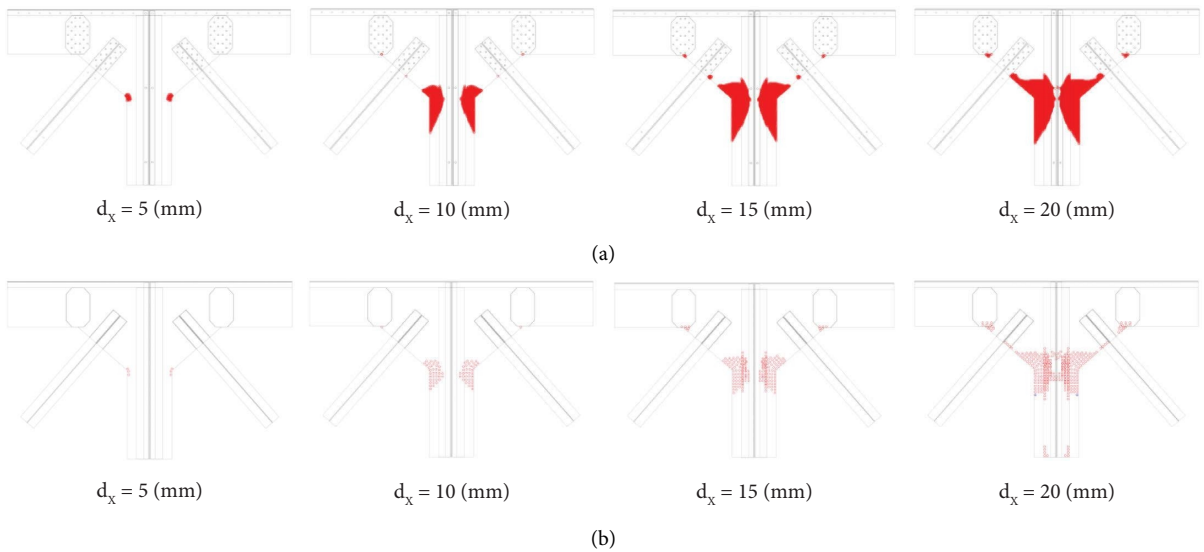


FIGURE 20: Plastic status of the fine model (a) and of the simplified model (b) at four different load steps.

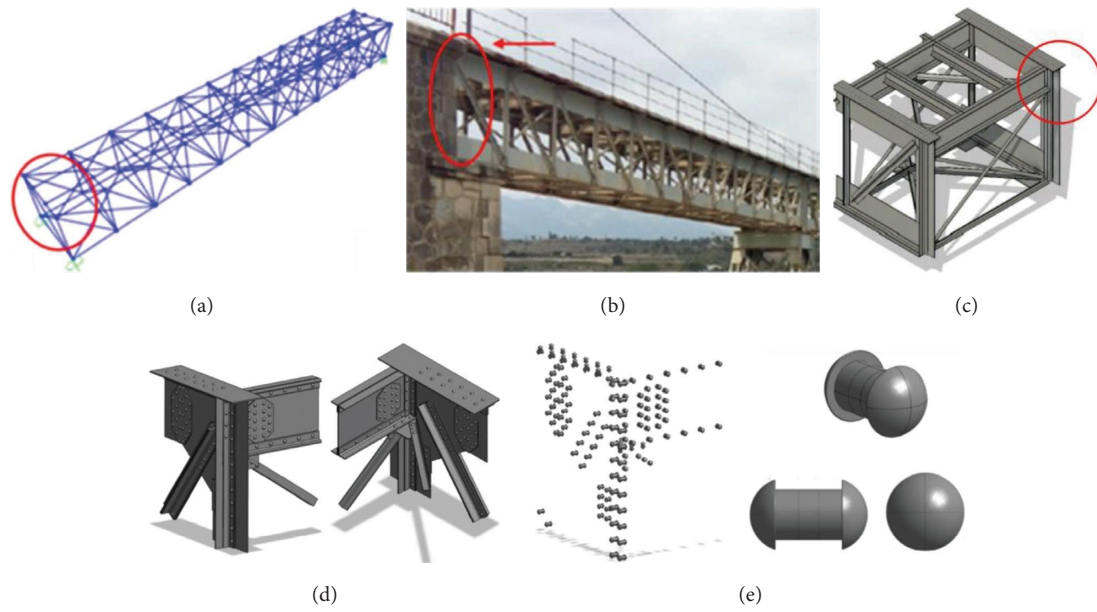


FIGURE 21: (a) Position of the node in the overall model of span 1 (support E1), (b) location of the node on the Viaduct, (c) position of the critical joint, (d) perspective views of the local model, and (e) modeled rivets.

forces, given the complexity of the geometry of the joint these stresses generate torsion on the wing of the crossbar. Analysis of the figures reveals maximum Von Mises stress values in the order of 400 MPa on the current and crossbar wing and less than 100 MPa on the rivets. Figure 23 shows the Plastic Status of the node in five different load steps: 20%, 40%, 60%, 80%, and 100%. The areas marked in red represent elements that have surpassed the elastic limit and are therefore in plasticity.

5. Image Processing-Based Damage Detection

In recent years, there was a progressive introduction at both European and International scales of many rules concerning nondestructive testing [53]. Such introduction made their de-facto equality to conventional and historically accepted tests possible. Furthermore, nondestructive tests provide their undisputed relevance not only as technical support but above all as a strong signal in favor of digital technologies and their systematic and standardized application. Radiographic inspection (X-ray and γ -ray) is applied in all industrial sectors where control is applied and, especially, in the field of welded joints [54]. However, the introduction of digital techniques requires the optimization of digital image processing techniques, objectives, level of accuracy, level of error, and image datasets, in order to automatically extract useful information about the cracks profile. For the selected case study, γ -ray inspections were carried out on a total of 160 joints (not all connections were analyzed) in which the presence of cracks, cavities, inclusions, fusion defects, and imperfections in shape and size were evaluated. The acquisition was carried out by the TÜV SÜD ATISAE laboratory (standard test procedure UNI EN ISO 5579). In general, the state of the connections is acceptable; however, small fissures have been identified in four zones of the bridge and the position of the cracks is

marked with red arrows as shown in Figure 24. It is worth noting that cracks 1 and 4 are located under the rivet cap or in the interior of the plate so by visual inspections it would not be possible to detect these cracks. Cracks 2 and 3 are centered on the cap of the rivet, so they probably could be related to the stage of fabrication process of the bridge. Damage detection by visual image processing requires the recognition and identification of both the observed object concerning the background and the specific defect. This involves the extraction of measurements characteristic of the defect regions, for example, the position of an object, orientation, area, perimeter, and length. Using image processing, a structuring element is applied to an input image, obtaining an output image of the same size. The image processing has been conducted through segmentation by thresholding, which is a process of partitioning an image into significant areas and it is carried out in a 3-step procedure, Figure 25. First, the damage photo is converted into grayscale and the thresholding algorithm is applied to create a binary image. The second step is noise removal, and finally, the edge detection step is used to identify different regions (regions associated with the crack are regions 3 and 4 in Figure 25). Once regions are identified it is possible to estimate the geometric parameters of the crack. The entire process was implemented through MATLAB's Image Processing Toolbox [55]. Sometimes a pre-elaboration is required to increase differences in average intensity and texture between different objects. Elementary operators of local textures include standard deviation, entropy filter, and range filter [56]. The simplest of these measures is the entropic operator applied here; Figures 26(a)–26(f) show the image process from the original image to the crack regions detection. The same procedure is applied to all the images; for each identified region, the geometric properties were assessed (position of barycenter, area, and major and minor axis).

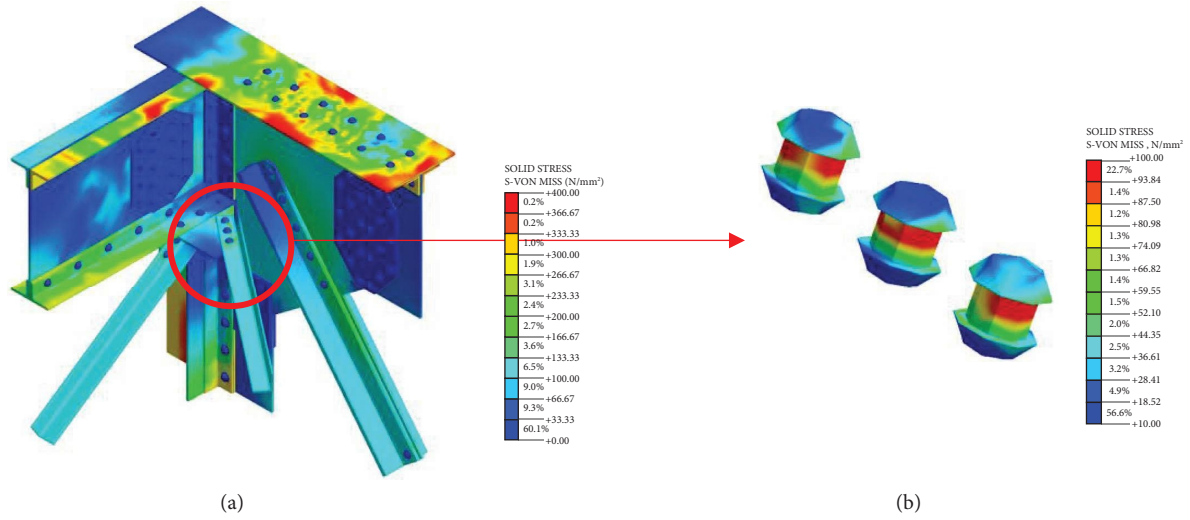


FIGURE 22: Von Mises stress obtained from SNL analysis on the solid model and on the rivets.

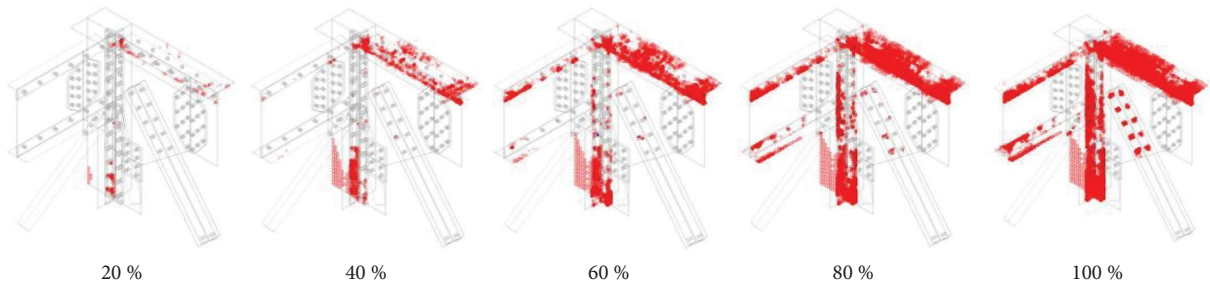


FIGURE 23: Plastic status of the solid model at different load steps.

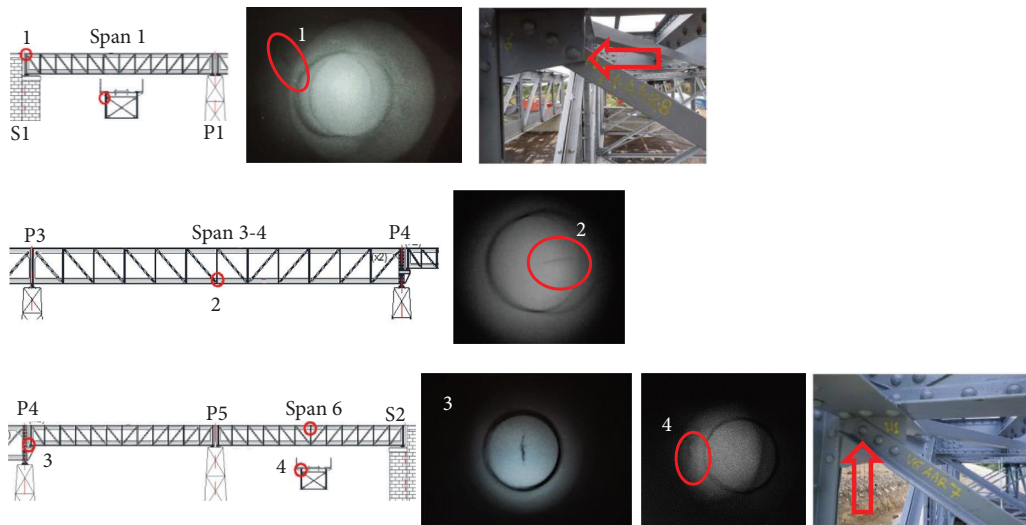


FIGURE 24: Bridge critical point where cracks were observed using gammagraphy.

A further deepening to estimate the goodness of the assessment has been carried out using the Intersection over Union index, IoU, i.e., the Jaccard index, which is the standard performance metric of semantic segmentation [57]. The IoU index is defined as the ratio of true positive and the

union of true positive, false positive, and false negative, which evaluates the similarity between the prediction and the ground truth. IoU metric, whose expressions have been reported in equations (18), quantifies the percent overall between the target mask and the prediction output by

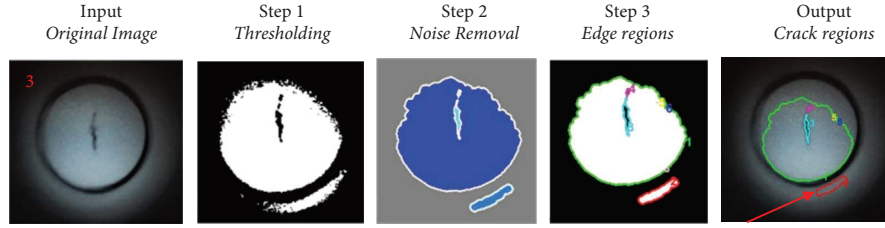


FIGURE 25: Architecture of the image processing-based crack detection applied to the 3rd image: original image, binary image, noise removal, detection of significant regions, and output image.

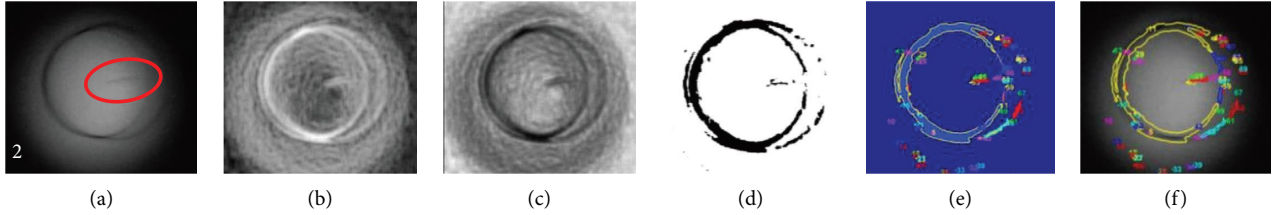


FIGURE 26: Architecture of the image processing process for crack detection applied to the 2nd image: (a) original image, (b) entropic filter, (c) complement, (d) binary image, (e) noise removal and edges outlined, and (f) regions detection.

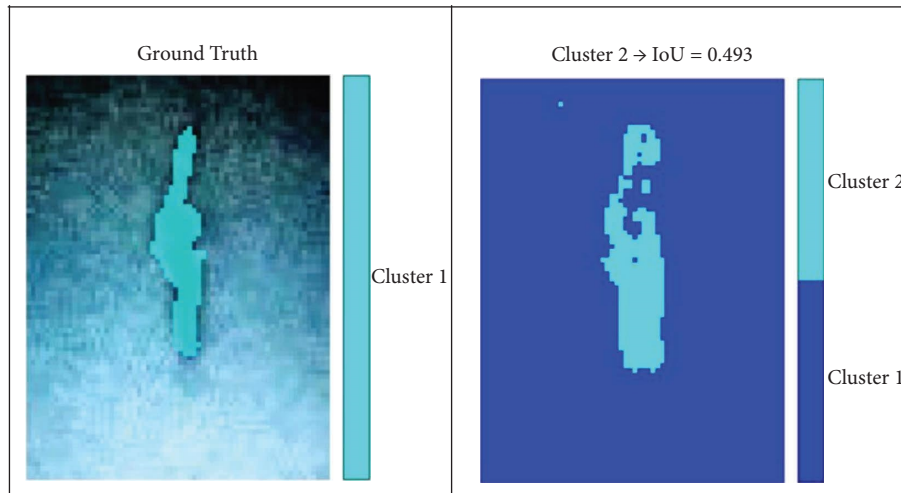


FIGURE 27: Performance of the thresholding algorithm using intersection over union IoU for Image 3.

measuring the number of pixels common between the target and the prediction masks divided by the total number of pixels present across both masks.

$$\text{IoU} = \frac{(\text{target} \cap \text{prediction})}{(\text{target} \cup \text{prediction})}. \quad (18)$$

The results in term of performance using the IoU index is shown in Figure 27 for Image 3.

6. Conclusions

This article deals with a procedure to identify damage in a steel truss railway bridge. Both model-based and data-

based procedures were implemented in this framework to highlight some advantages and drawbacks of these two approaches. Model-based procedures tend to be limited in providing detailed knowledge about the stress states of the joint. Distorsional and secondary phenomena related to the steel deck behavior, that are generally neglected or simply not considered in traditional analysis, can play a key role in fatigue damaging estimation. These phenomena include the loop effect, the clamping force, the presence of residual stresses resulting from the rivet installation process, and thermal contraction. The presence of these phenomena affects the crack location and the path of fatigue cracks at rivet holes. On the other hand, data can help to better understand the local damage and its characterization. For these reasons,

the approach is based on an appropriate interconnection between different experimental and numerical analysis techniques (methods for identification of the modal models and flexibility; data-based stochastic procedures, SSI; and image processing). These analyses are finalized to obtain a realistic and reliable assessment of the damage due to fatigue of the main critical components, through mechanical models describing the phenomenon, calibrated on observed experimental data. The methodology requires technical knowledge derived from various scientific fields concerning the behavior of steel bridges: from computational modeling to dynamic identification and from model updating techniques to image processing for damage identification. A combination of nondestructive data acquisition using gamma-ray followed by precise image analysis is necessary to obtain an accurate quantitative analysis of cracks. Image analysis was used to characterize the 2D nature of cracks formed in the steel joints. Image analysis was instrumental in segmenting the cracks to obtain accurate measurements of length, thickness, and other morphological information. The discussion of a real case study, the Quisi bridge, enriches the discussion and highlights the possible application of such approach. Global analysis and FE updating from dynamic measurements allowed to obtain a reliable prediction of the portion of the truss structure in which damage is localized. Refined FE models and nonlinear analysis have delineated a reasonable scenario of cracks for fatigue effects which have been compared with data coming from γ -ray pictures' image processing.

Data Availability

No public datasets have been used.

Conflicts of Interest

The authors declare that they have no conflicts of interest.

Acknowledgments

This work was financed through a European Project funded by the Research Fund for Coal and Steel under grant agreement no. 800687 (DESDEMONA EU Project).

References

- [1] F. Moreu, J. LaFave, and B. Spencer, "Structural health monitoring of railroad bridges – research needs and preliminary results," *ASCEE Structures Congress*, vol. 19, pp. 2141–2152, 2012.
- [2] C. W. Kim, S. Kitauchi, K. Chang, P. J. Mcgetrick, K. Sugiura, and M. Kawatani, "Structural damage diagnosis of steel truss bridges by outlier detection," in *Proceedings of the 11th International Conference on Structural Safety and Reliability 2014 ICOSSAR*, pp. 4631–4638, San Francisco, CA, USA, June 2014.
- [3] M. Mehrjou, M. Khaji, H. Moharrami, and A. Bahreininejad, "Damage detection of truss bridge joints using Artificial Neural Network," *Journal of Expert System with Applications*, vol. 35, no. 3, pp. 1122–1131, 2008.
- [4] A. M. Scianna and R. Christenson, "Probabilistic structural health monitoring method applied to the bridge health monitoring benchmark problem," *Transportation Research Record: Journal of the Transportation Research Board*, vol. 2131, no. 1, pp. 92–97, 2009.
- [5] Z. R. Lu and J. K. Liu, "Identification of both structural damages in bridge deck and vehicular parameters using measured dynamic responses," *Computers & Structures*, vol. 89, no. 13-14, pp. 1397–1405, 2011.
- [6] B. Moaveni, S. Hurlebaus, and F. Moon, "Special issue on real-world applications of structural identification and health monitoring methodologies," *Journal of Structural Engineering*, vol. 139, no. 10, pp. 1637–1638, 2013.
- [7] R. H. Scott, P. Banerji, S. Chikermane et al., "Commissioning and evaluation of a fiber-optic sensor system for bridge monitoring," *IEEE Sensors Journal*, vol. 13, no. 7, pp. 2555–2562, 2013.
- [8] T. You, P. Gardoni, and S. Hurlebaus, "Iterative damage index method for structural health monitoring," *Structural Monitoring and Maintenance*, vol. 1, no. 1, pp. 89–110, 2014.
- [9] S. Beskhyroun, T. Oshima, and S. Mikami, "Wavelet-based technique for structural damage detection," *Structural Control and Health Monitoring*, vol. 17, pp. 473–494, 2010.
- [10] C. Bowe, P. Quirke, D. Cantero, and E. J. O'Brien, "Drive-by structural health monitoring of railway bridges using train mounted accelerometers," in *Proceedings of the 5th ECCOMAS Thematic Conference on Computational Methods in Structural Dynamics and Earthquake Engineering 2015*, Crete Island, Greece, May 2015.
- [11] I. Gonzalez and R. Karoumi, "BWIM aided damage detection in bridges using machine learning," *Journal of Civil Structural Health Monitoring*, vol. 5, pp. 715–725, 2015.
- [12] F. Moreu, H. Jo, J. Li et al., "Dynamics assessment of timber railroad bridges using displacements," *Journal of Bridge Engineering*, vol. 20, no. 10, Article ID 04014114, 2012.
- [13] R. V. Farahani and D. Penumadu, "Damage identification of a full-scale five-girder using time-series analysis of vibration data," *Engineering Structures*, vol. 115, pp. 129–139, 2016.
- [14] R. C. George, J. Posey, A. Gupta, S. Mukhopadhyay, and S. K. Mishra, "Damage detection in railway bridges under moving train load," *Model Validation and Uncertainty Quantification*, vol. 3, pp. 349–725, 2017.
- [15] F. P. Kopsaftopoulos and S. Fassois, "Vibration-based health monitoring for a lightweight truss structure: experimental assessment of several statistical time series methods," *Mechanical Systems and Signal Processing*, vol. 24, no. 7, pp. 1977–1997, 2010.
- [16] L. Wang, T. H. Chan, D. P. Thambiratnam, A. C. C. Tan, and C. J. L. Cowled, "Correlation-based damage detection for complicated truss bridges using multi-layer genetic algorithm," *Advances in Structural Engineering*, vol. 15, no. 5, pp. 693–706, 2012.
- [17] S. C. Siriwardane, "Vibration measurement-based simple technique for damage detection of truss bridges: a case study," *Case Studies in Engineering Failure Analysis*, vol. 4, pp. 50–58, 2015.
- [18] M. R. Azim and M. Gül, "Damage detection framework for truss railway bridges utilizing statistical analysis of operational strain response," *Structural Control and Health Monitoring*, vol. 27, no. 8, p. 2573, 2020a.
- [19] M. R. Azim and M. Gül, "Damage detection of steel truss railway bridges using operational vibration data," *Journal of Structural Engineering*, vol. 146, no. 3, Article ID 04020008, 2020.

- [20] M. R. Azim and M. Gül, "Damage detection of steel girder railway bridges utilizing operational vibration response," *Structural Control and Health Monitoring*, vol. 26, no. 11, p. 2447, 2019.
- [21] M. Diaferio, V. Sepe, and G. Bellizzi, "Modal identification of localised damage in beams and trusses: experimental and numerical results," *International Journal of Advanced Structural Engineering*, vol. 11, no. 4, pp. 421–437, 2019.
- [22] B. Peeters and G. De Roeck, "One-year monitoring of the z24-bridge: environmental influences versus damage events," in *Proceedings of the IMAC 18 the International Modal Analysis Conference*, pp. 1570–1576, San Antonio, TX, USA, February 2001.
- [23] M. N. Cerri and F. Vestroni, "Detection of damage in beam subjected to diffused cracking," *Journal of Sound and Vibration*, vol. 234, no. 2, pp. 259–276, 2000.
- [24] V. Gattulli, E. Lofrano, A. Paolone, and F. Potenza, "Measured properties of structural damping in railway bridges," *Journal of Civil Structural Health Monitoring*, vol. 9, no. 5, pp. 639–653, 2019.
- [25] F. Potenza, G. Castelli, V. Gattulli, and E. Ottaviano, "Integrated process of image and acceleration measurements for damage detection," *EURODYN*, vol. 25, 2017.
- [26] F. Potenza, C. Rinaldi, E. Ottaviano, and V. Gattulli, "A robotics and computer-aided procedure for defect evaluation in bridge inspection," *Journal of Civil Structural Health Monitoring*, vol. 10, no. 3, pp. 471–484, 2020.
- [27] P. Wang and H. Huang, "Comparison analysis on present image-based crack detection methods in concrete structures," *Proceedings of 3rd International Congress on Image and Signal Processing CISP*, vol. 5, pp. 2530–2533, 2010.
- [28] A. M. A. Talab, Z. Huang, F. Xi, and L. HaiMing, "Detection crack in image using Otsu method and multiple filtering in image processing techniques," *Optik*, vol. 127, no. 3, pp. 1030–1033, 2016.
- [29] R. S. Adhikari, O. Moselhi, and A. Bagchi, "Image-based retrieval of concrete crack properties for bridge inspection," *Automation in Construction*, vol. 39, pp. 180–194, 2014.
- [30] S. Y. Alam, A. Loukili, F. Grondin, and E. Rozière, "Use of the digital image correlation and acoustic emission technique to study the effect of structural size on cracking of reinforced concrete," *Engineering Fracture Mechanics*, vol. 143, pp. 17–31, 2015.
- [31] Y. C. Zang, G. Y. Xu, and J. Cui, "System used to detect steel wire rope based on X-ray digital imaging technology," *Image Technology*, vol. 2, pp. 33–39, 2008.
- [32] P. C. Peng and C. Y. Wang, "Use of gamma rays in the inspection of steel wire ropes in suspension bridges," *NDT and E International*, vol. 75, pp. 80–86, 2015.
- [33] A. Deraemaeker, E. Reynders, G. De Roeck, and J. Kullaa, "Vibration-based structural health monitoring using output-only measurements under changing environment," *Mechanical Systems and Signal Processing*, vol. 22, no. 1, pp. 34–56, 2008.
- [34] D. Foti, V. Gattulli, and F. Potenza, "Output-only identification and model updating by dynamic testing in unfavorable conditions of a seismically damaged building: output-only identification of a seismically damaged building," *Computer-Aided Civil and Infrastructure Engineering*, vol. 29, no. 9, pp. 659–675, 2014.
- [35] M. Crognale, V. Gattulli, S. Ivorra, and F. Potenza, "Dynamics and damage sensitivity of the Quisi steel truss bridge," in *ANCRiSST 2019 Procedia: 14th International Workshop on Advanced Smart Materials and Smart Structures Technology*, vol. 45, Sapienza Università Editrice, Rome, Italy, 2019.
- [36] M. Crognale, V. Gattulli, A. Paolone, and F. Potenza, "A procedure for damage identification in a steel truss," *XXIV Congresso AIMETA 2019*, Associazione Italiana di Meccanica Teorica e Applicata, , vol. 15, Rome, Italy, 2019.
- [37] M. Crognale, V. Gattulli, S. Ivorra, and F. Potenza, "An integrated vibration-image procedure for damage identification in steel trusses," in *Proceedings of the XI International Conference on Structural Dynamics, EURODYN*, pp. 23–25, Florence, Italy, June 2020.
- [38] Eurocode 1, *EN1991-2: Actions on Structures - Part 2: Traffic Loads on Bridges*, CEN, Brussels, Belgium, 2003.
- [39] E. Reynders, M. Schevenels, and G. De Roeck, *MACEC: A Matlab Toolbox for Experimental and Operational Analysis*, KU Leuven, Leuven, Belgium, 2008.
- [40] B. Peeters and G. De Roeck, "Reference-based stochastic subspace identification in Civil Engineering," *Inverse Problems in Engineering*, vol. 8, no. 1, pp. 47–74, 2000.
- [41] B. Peeters and G. De Roeck, "Reference-based stochastic subspace identification for output-only modal analysis," *Mechanical Systems and Signal Processing*, vol. 13, no. 6, pp. 855–878, 1999.
- [42] Y. Gao, B. F. Spencer, D. Bernal, and D. Bernal, "Experimental verification of the flexibility-based damage locating vector method," *Journal of Engineering Mechanics*, vol. 133, no. 10, pp. 1043–1049, 2007.
- [43] T. Nguyen-Thoi, A. Tran-Viet, N. Nguyen-Minh, T. Vo-Duy, and V. Ho-Huu, "A combination of damage locating vector method (DLV) and differential evolution algorithm (DE) for structural damage assessment," *Frontiers of Structural and Civil Engineering*, vol. 12, no. 1, pp. 92–108, 2018.
- [44] R. J. Allemang and D. L. Brown, "A correlation coefficient for modal vector analysis," in *Proceedings of the 1st International Modal Analysis Conference, IMAC*, Copenhagen, Denmark, May 1982.
- [45] ATC, "Instrucción para redactar los proyectos de puentes metálicos," 1902, <http://normativa.itafec.com/obras-de-paso-puentes-estructuras/ES.07.04.007.RD.pdf>.
- [46] Librería Técnica Bellisco, *La estructura metálica hoy R Arguelles Álvarez*, Librería Técnica Bellisco, Madrid, Spain, 2023.
- [47] V. Sangiorgio, A. Nettis, G. Uva, F. Pellegrino, H. Varum, and J. M. Adam, "Analytical fault tree and diagnostic aids for the preservation of historical steel truss bridges," *Engineering Failure Analysis*, vol. 133, Article ID 105996, 2022.
- [48] S. W. Doebling, C. R. Farrar, M. B. Prime, and D. W. Shevitz, *Damage Identification and Health Monitoring of Structural and Mechanical Systems from Changes in Their Vibration Characteristics: A Literature Review*, Technical Report Los Alamos National Laboratory, Los Alamos, NM, USA, 1996.
- [49] D. Capecchi and F. Vestroni, "Identification of finite element models in structural dynamics," *Engineering Structures*, vol. 15, no. 1, pp. 21–30, 1993.
- [50] R. Jafarkhani and S. Masri, "Finite element model updating using evolutionary strategy for damage detection," *Computer-Aided Civil and Infrastructure Engineering*, vol. 26, no. 3, pp. 207–224, 2011.
- [51] J. E. Mottershead and M. I. Friswell, "Model updating in structural dynamics: a Survey," *Journal of Sound and Vibration*, vol. 167, no. 2, pp. 347–375, 1993.
- [52] F. Valvona, J. Toti, V. Gattulli, and F. Potenza, "Effective seismic strengthening and monitoring of a masonry vault by using glass fiber reinforced cementitious matrix with

- embedded fiber bragg grating sensors,” *Composites Part B: Engineering*, vol. 113, pp. 355–370, 2017.
- [53] V. Gattulli and L. Chiaramonte, “Condition assessment by visual inspection for a bridge management system,” *Computer-Aided Civil and Infrastructure Engineering*, vol. 20, no. 2, pp. 95–107, 2005.
- [54] M. Lukic, A. Nussbaumer, H. P. Günther et al., “Assessment of existing steel structures - recommendations for estimation of the remaining fatigue life,” *Procedia Engineering*, vol. 66, pp. 3–11, 2003.
- [55] The MathWorks Inc, *Image Processing Toolbox Version 3.2 Run under Matlab 6.5*, The MathWorks Inc, Natick, Massachusetts, USA, 2023.
- [56] C. Solomon and T. Breckon, *Foundamentals of Digital Image Processing: A Practical Approach with Examples in Matlab*, Wiley-Bleckwell, Hoboken, NJ, USA, 2011.
- [57] M. Crognale, M. De Iuliis, C. Rinaldi, and V. Gattulli, “Damage detection with image processing: a comparative study,” *Special issue on Computer Vision Empowering Earthquake Engineering and Engineering Vibration of EEEV*, vol. 12, pp. 707–715, 2014.